

2009-01-01

Microstructural Characterization of Overaged GTD-111 HP Turbine Buckets

Oscar Quintero

University of Texas at El Paso, oquintero@miners.utep.edu

Follow this and additional works at: https://digitalcommons.utep.edu/open_etd



Part of the [Materials Science and Engineering Commons](#), and the [Mechanics of Materials Commons](#)

Recommended Citation

Quintero, Oscar, "Microstructural Characterization of Overaged GTD-111 HP Turbine Buckets" (2009). *Open Access Theses & Dissertations*. 2758.

https://digitalcommons.utep.edu/open_etd/2758

This is brought to you for free and open access by DigitalCommons@UTEP. It has been accepted for inclusion in Open Access Theses & Dissertations by an authorized administrator of DigitalCommons@UTEP. For more information, please contact lweber@utep.edu.

Microstructural Characterization of Overaged
GTD-111 HP Turbine Buckets

OSCAR QUINTERO SOLTERO

Department of Metallurgical and Materials Engineering

APPROVED:

Stephen W. Stafford, Ph.D., Chair

Lawrence E. Murr, Ph.D.

John Walton, Ph.D.

Patricia D. Witherspoon, Ph.D.
Dean of the Graduate School

Copyright
by
Oscar Quintero Soltero
2009

Microstructural Characterization of Overaged
GTD-111 HP Turbine Buckets

by

OSCAR QUINTERO SOLTERO, B.S. Electrical Engineering

THESIS

Presented to the Faculty of the Graduate School of

The University of Texas at El Paso

in Partial Fulfillment

of the Requirements

for the Degree of

MASTER OF SCIENCE

Department of Metallurgical and Materials Engineering

THE UNIVERSITY OF TEXAS AT EL PASO

December 2009

Acknowledgements

I would like to thank my parents and sister for their invaluable education and support ever since I was a child never giving up on me and always encouraging me in every stage of my life. I would also like to thank my mentor, Professor, and thesis advisor: Dr. Steve Stafford. I was introduced to a chapter called Failure Analysis in Materials in the Introduction to Materials Science and Engineering class in the Spring 2004 semester and I have never looked back since. This chapter changed my life and I do not have any words to describe what it has done to me personally, academically, and professionally. I would also like to thank the Department of Metallurgy and Materials Engineering's Faculty and Staff at UTEP for their support and knowledge throughout my graduate degree. I would like to also thank my wife, Adriana Flores, for her love and patience throughout this process and Ms. Sara Gaytán for all the help and technical support offered during this process.

Abstract

Superalloys are metallic materials that exhibit excellent mechanical strength and creep resistance at high temperatures. They have good surface stability and are corrosion resistant. Superalloys are mostly used in the aerospace industry, gas turbine engines and blades (hot zones of gas turbines), and where extreme heat is encountered. The focus of this research was on the GTD-111 Ni-base superalloy, which is a General Electric (GE) proprietary superalloy mostly used in gas turbine blades with the form of high pressure or first stage buckets. This alloy features better mechanical properties, creep resistance, and a higher stress rupture temperature than the commonly used Inconel 738LC Ni-base superalloy.

The purpose of this research was to characterize the microstructural differences between two different sections (airfoil and shank) of a GTD-111 General Electric Frame 3/2 Model “J” Dry Low NO_x Unit Stage 1 bucket. This research was divided into several stages: a) microstructure, b) elemental Composition determination using energy dispersive x-ray spectroscopy (EDS), c) microhardness testing, d) gamma-prime (γ') diameter using the scanning electron microscope (SEM), and e) transmission electron microscopy (TEM). The buckets had been in service for 48, 064 hours at an approximate service temperature of 1700 – 1800 °F.

Microstructural changes were examined by the use of metallography, scanning electron microscopy, transmission electron microscopy, and microhardness testing in the airfoil and shank sections of the turbine buckets. These techniques provided the means to establish specific microstructural alteration which included:

- 1.) γ' coarsening and particle coalescence;
- 2.) the essence of solute re-distribution between the γ and γ' phases, and MC carbide decomposition;
- 3.) the apparent thermal modification of γ' eutectic structures;
- 4.) and the strengthening of the trailing edge regions of the airfoils.

The overall γ' coarsening and coalescence occurs mainly by the Ostwald ripening effect and follows the Lifshitz, Sloyozov, and Wagner theory. All of the elemental changes in the microstructure

suggest that vacancy diffusion took place and could have contributed to the strengthening (higher hardness and tensile strength) of the trailing edge of the airfoil. It is important to mention that the material's performance depends on the ability to retain its original microstructural features during service, since preserving this microstructural state represents an optimum design condition.

Metallographic inspection by replication can be used to analyze the microstructural changes the buckets have undergone. Such technique is non-destructive and can be used in preventive maintenance routines to assess the microstructural degradation and determine if component can continue in service. Future work includes a more in depth microstructural investigation for different service conditions to help determine a more approximate rate of degradation of the γ' phase. Also, any future work would have to entail creep rupture testing to confirm residual elevated temperature properties.

Table of Contents

Acknowledgements.....	iv
Abstract.....	v
Table of Contents.....	vii
List of Tables	ix
List of Figures.....	x
Chapter 1: Introduction to Superalloys.....	1
1.1 Introduction.....	1
1.2 Introduction to Nickel-Based Superalloys.....	1
Chapter 2: Introduction to the GTD-111 Superalloy	3
2.1 Microstructure.....	5
2.1.1 Gamma Phase (γ).....	5
2.1.2 Gamma Prime (γ') Phase	6
2.1.3 Gamma Double Prime (γ'')	6
2.1.4 Carbides	7
Chapter 3: Experimental Program.....	9
3.1 Sample Preparation	10
3.2 Microstructural Analysis	10
3.3 Phase Elemental Composition Determination	11
3.4 Hardness	11
3.5 Gamma Prime (γ') Diameter	11
3.6 Transmission Electron Microscopy (TEM).....	11
Chapter 4: Results.....	13
4.1 Microstructural Analysis	13
4.2 Phase Elemental Composition (EDS) Results	18
4.3 Hardness Results.....	23
4.4 Gamma Prime (γ') Diameter	26
4.5 Transmission Electron Microscopy (TEM).....	29

Chapter 5: Discussion.....	35
Chapter 6: Conclusions.....	41
References.....	44
Curriculum Vita.....	48

List of Tables

Table 1.1 - The roles of alloying elements in Ni-base superalloys.....	2
Table 2.1 – Chemical composition of the GTD-111 superalloy, Inconel 738LC, and René 80	3

List of Figures

Figure 2.1: Stress rupture comparison between bucket materials (Inconel 738 and GTD-111)	4
Figure 2.2: Steady-state creep rate as a function of rupture time of GTD-111 and Inconel 738LC and time to tertiary creep versus minimum creep rate in GTD-111 and Inconel 738LC	4
Figure 2.3: Solidification sequence of GTD-111 superalloy.....	8
Figure 3.1: Components of a Gas Turbine Bucket.....	9
Figure 3.2: Bucket used for this study.....	10
Figure 4.1: $M_{23}C_6$ carbides were found along the grain boundaries.....	13
Figure 4.2: $M_{23}C_6$ carbides were found along the grain boundaries. Dispersed γ' was found along the γ matrix.....	13
Figure 4.3: Dispersed γ' was found along the γ matrix. γ' islands are present in some areas of the γ matrix along the grain boundary	14
Figure 4.4: γ' islands dispersed throughout γ matrix. γ' islands are also present on the grain boundary...	14
Figure 4.5: Eutectic Phase	15
Figure 4.6: Dispersed γ' throughout γ matrix.....	15
Figure 4.7: Eutectic phase and MC carbide islands were found in γ matrix.....	15
Figure 4.8: $M_{23}C_6$ carbides are present on the grain boundaries. γ' islands are also present in the γ matrix and on the grain boundary as well.....	16
Figure 4.9: γ' island is located at grain boundary. Dispersed γ' is also present on the γ matrix. Eutectic phases and γ' islands are also present on the matrix. MC carbides are also precipitated in γ matrix	16
Figure 4.10: Dispersed γ' in the γ matrix. $M_{23}C_6$ carbides are also present along grain boundary.....	17

Figure 4.11: Dispersed γ' is present on the γ matrix. $M_{23}C_6$ Carbides and γ' islands were also present in the grain boundaries	17
Figure 4.12: γ matrix qualitative chemical composition. Notice the higher presence of chromium (Cr), aluminum (Al), titanium (Ti) and tungsten (W) in the airfoil sample	18
Figure 4.13: γ' qualitative chemical composition. Notice the higher presence of aluminum (Al), tungsten (W), and titanium (Ti) in the airfoil sample	19
Figure 4.14: MC carbide qualitative chemical composition. Notice a higher presence of chromium (Cr) in the airfoil sample.....	20
Figure 4.15: Eutectic phase qualitative chemical composition. Notice a lower presence of titanium (Ti), aluminum (Al), and tungsten (W) in the airfoil sample.....	21
Figure 4.16: Eutectic phase qualitative chemical composition. Notice a lower presence of aluminum (Al) and titanium (Ti) in the airfoil sample. Shank sample shows a higher presence of tungsten (W).	22
Figure 4.17: Shank hardness profile cross section	23
Figure 4.18: Shank hardness profile results. The results above portray the alloy's hardness as in new condition due to the lack of heat exposure during service	23
Figure 4.19: Airfoil microhardness profile cross sectional for Area 1, Area 2, and Area 3.....	24
Figure 4.20: Airfoil hardness profile results for Area 1, Area 2 and Area 3. Areas 2 and 3 have similar hardness results while Area 1 was the area that showed a hardness difference between the analyzed areas.....	24
Figure 4.21: Hardness (HV) comparison between shank and the three areas that were measured in the airfoil. The Area 1 of the airfoil showed a higher hardness than the shank and the rest of the airfoil's areas.....	25
Figure 4.22: Rockwell hardness equivalent comparison between airfoil and shank	25

Figure 4.23: Gamma prime (γ') diameter in shank. See Figure 4.45 for comparison	26
Figure 4.24: Gamma prime (γ') in airfoil. Notice in lower right image that the gamma prime (γ') coarsens and joins other gamma prime (γ') phases creating a film formation, which weakens the alloy. See Figure 4.45 for comparison	27
Figure 4.25: Gamma prime (γ') diameter comparison. Airfoil sample features a larger gamma prime (γ') diameter than the shank sample, which confirms that the gamma prime (γ') of the airfoil gets coarser (compared to the shanks) after exposure to high temperatures. This also confirms that the airfoil's gamma prime (γ') gets coarser at a faster rate.....	28
Figure 4.26: TEM micrograph of shank sample. Notice cuboidal γ' and dispersed γ'' in γ matrix. Electron diffraction pattern for γ' (FCC). B = [001].....	29
Figure 4.27: TEM micrograph of shank sample. Notice cuboidal γ' and dispersed γ'' in γ matrix along with an MC carbide island. Electron diffraction pattern for γ' (FCC). B = [001].....	29
Figure 4.28: TEM micrograph of shank sample. TEM micrograph of shank sample. Notice cuboidal γ' and dispersed γ'' in γ matrix along with an $M_{23}C_6$ carbide. Electron diffraction pattern. B = [001].	30
Figure 4.29: TEM micrograph of shank sample. Notice cuboidal γ' and dispersed γ'' in γ matrix along with an MC carbide island. Electron diffraction pattern for γ' (FCC). B = [110] special reflection	30
Figure 4.30: TEM micrograph of shank sample. Notice cuboidal γ' and dispersed γ'' in γ matrix along with an MC carbide island. Electron diffraction pattern for MC carbide (cubic) and γ'' (bct). B = [001]	31
Figure 4.31: TEM micrograph of airfoil sample. Notice spherical γ' in γ matrix. Electron diffraction pattern for γ' (FCC). B = [111].	32

Figure 4.32: TEM micrograph of airfoil sample. Notice spherical γ' and $M_{23}C_6$ in γ matrix. Electron diffraction pattern for γ' (FCC). $B = [100]$ outer portion of pattern.	32
Figure 4.33: TEM micrograph of airfoil sample. Notice spherical γ' and $M_{23}C_6$ in γ matrix. Electron diffraction pattern for γ' (FCC). $B = [013]$ outer portion of pattern.	33
Figure 4.34: TEM micrograph of airfoil sample. Notice spherical γ' in γ matrix. Electron diffraction pattern for γ' (FCC). $B=[001]$	33
Figure 4.35: TEM micrograph of airfoil sample. Notice spherical γ' , γ'' , and $M_{23}C_6$ in γ matrix. [27]. Electron diffraction pattern for γ'' (bct).	34
Figure 5.36: Tensile strength comparison between areas of airfoil and shank sections.....	37
Figure 5.37: Correlation of average size of γ' precipitates with time during service conditions according to LSW theory.....	39
Figure 5.38 Correlation of average size of γ' precipitates with time during service conditions in exponential behavior simulating actual service conditions of 150,000 hrs.....	40

Chapter 1: Introduction to Superalloys

1.1 INTRODUCTION

Superalloys are metallic materials that exhibit excellent mechanical strength and creep resistance at high temperatures. They have good surface stability and are corrosion resistant. Superalloys are mostly used in the aerospace industry, gas turbine engines and blades (hot zones of gas turbines), and where extreme heat is encountered. The common superalloys are based on nickel (Ni), cobalt (Co), and iron (Fe) [1]. The focus of this research is on nickel-based superalloys since the GTD-111 superalloy is part of this group.

1.2 INTRODUCTION TO NICKEL-BASED SUPERALLOYS

Nickel-based superalloys were introduced in the 1940s due to the need of a material that had a high temperature tensile strength, high creep rupture strength, and was oxidation resistant. The most common applications for Nickel-based superalloys are in the aircraft engine industry and industrial turbines, where temperatures range from 1200 – 2000 °F (650 – 1200 °C) and a creep rupture strength of a range of 20,000 – 50,000 h life [2]. The Nickel based superalloys replaced the austenitic stainless steels due to better creep resistance.

The microstructure of Nickel-based superalloys consists of an FCC solid solution matrix γ (mostly austenite), carbides, and the intermetallic phase γ' . These alloys are strengthened by aluminum, titanium, niobium, columbium, and tantalum, which combined with nickel, forms the FCC γ' phase. Also, refractory elements such as molybdenum, tungsten, tantalum, chromium, and cobalt help prevent local hot corrosion. See Table 1 for the roles of the alloying elements in Nickel-base superalloys. Strength is enhanced by elements in solid solution. Usually, the most effective are molybdenum, tungsten, and chromium. They form carbides which contribute to grain boundary strengthening, although if an excess of carbides is present, then the grain boundaries weaken. Aluminum and chromium also provide oxidation resistance, while chromium and titanium are effective against hot-corrosion resistance [3].

Table 1.1 The roles of alloying elements in Ni-base superalloys [4]

The roles of alloying elements in Ni-base superalloys

	Ni	Co	Fe	Cr	Mo, W	Nb, Ta, Ti	Al	C, B, Zr, Hf
Solid solution	×	×	×	×	×			
Grain boundary								×
Precipitation						×	×	
Carbide formers				×	×	×		
Oxide formers				×			×	

Chapter 2: Introduction to the GTD-111 Superalloy

The GTD-111 superalloy is a General Electric (GE) proprietary Nickel-based superalloy mostly used in gas turbines with the form of high pressure or first stage buckets. This alloy was patented in the 1970s and introduced in the market around the 1980s. GTD-111 is mostly used in directionally solidified (DS) buckets and equiaxed buckets. The differences between the DS and the equiaxed GTD-111 are that the creep life is increased in the DS and has a greater thermal fatigue than the equiaxed GTD-111 [5]. Table 2.1 shows the chemical composition of the GTD-111. Also, the GTD-111 superalloy is considered to be a modified version of GE's commonly used René 80 Ni-based superalloy.

Table 2.1 – Chemical composition of the GTD-111 superalloy, Inconel 738LC, and René 80 [6, 7]

(Weight Percentages)

	Cr	Ni	Co	Fe	W	Mo	Ti	Al	Cb	V	C	B	Ta	Zr
GTD111	14	Bal	9.5	-	3.8	1.5	4.9	3.0	-	-	0.10	0.01	2.8	-
René 80	14	Bal	9.5	-	4.0	4.0	5.0	3.0	-	-	0.17	0.015	-	0.03
IN738LC	16.0	Bal	8.3	-	2.6	1.70	3.38	3.4	-	-	0.11	0.01	1.7	-

Figure 2.1 shows that the GTD-111 alloy ruptures at approximately 20°C more than the commonly used Inconel 738 (for both buckets and nozzles).

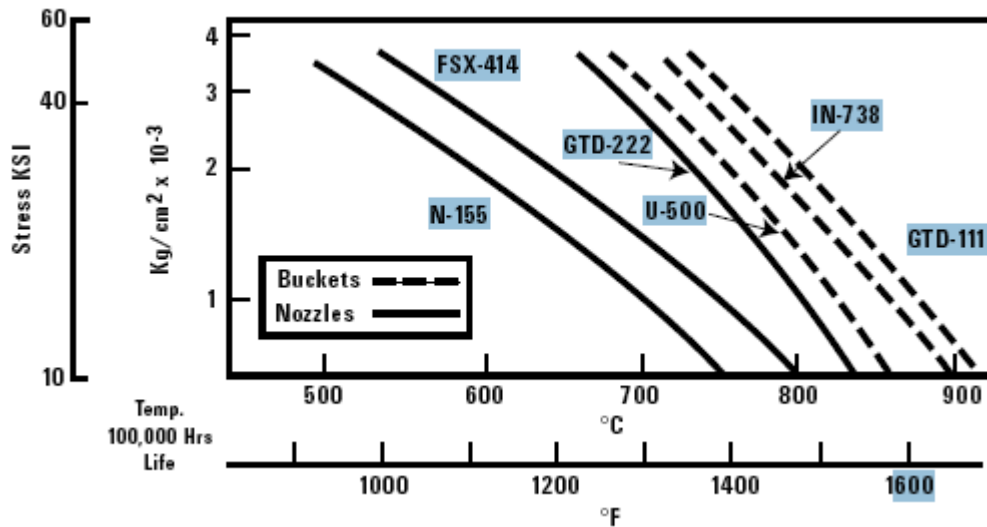


Figure 2.1 – Stress rupture comparison between bucket materials (Inconel 738 and GTD-111) [8].

Figure 2.2 shows the steady-state creep rate as a function of rupture time of GTD-111 and Inconel 738LC and time to tertiary creep versus minimum creep rate in GTD-111 and Inconel 738LC. Both graphs confirm that the GTD-111 alloy creep rate is more stable than the Inconel 738LC, thus making it a better alternative than the previously used Inconel 738LC alloy.

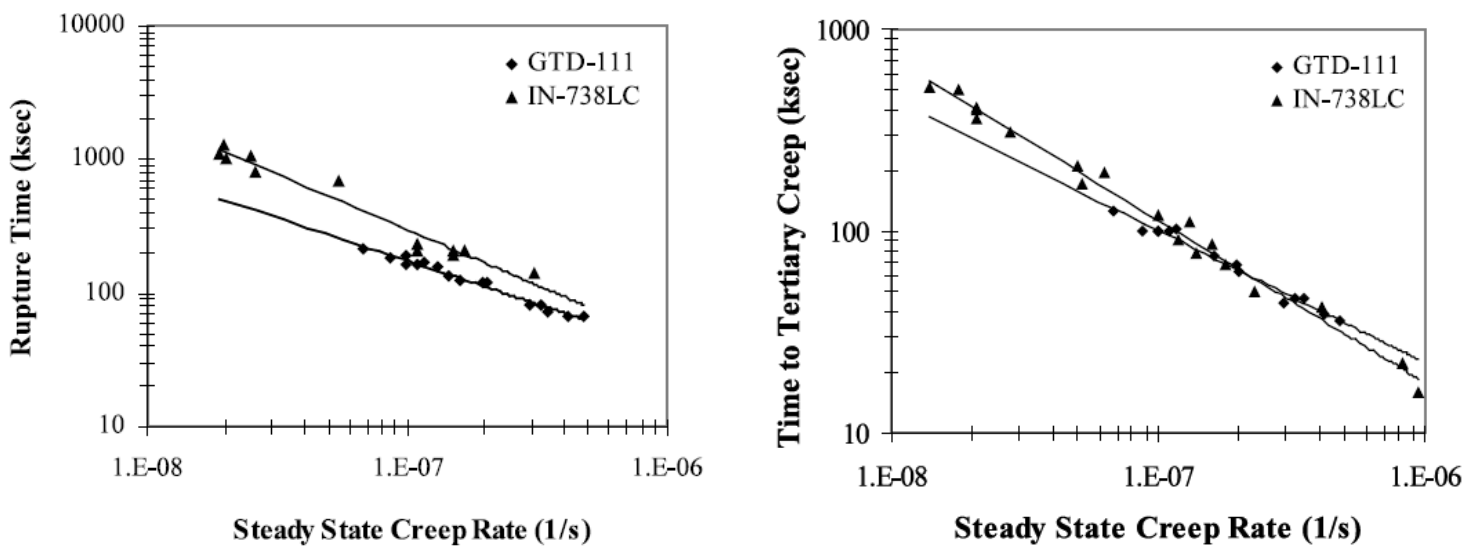


Figure 2.2 – Steady-state creep rate as a function of rupture time of GTD-111 and Inconel 738LC and time to tertiary creep versus minimum creep rate in GTD-111 and Inconel 738LC. [9]

The strength of this Ni-based superalloy is achieved through precipitation hardening, which consists of dispersing extremely small uniform particles of a second phase (γ' and γ'') and carbides within the original matrix, which also provide dispersion strengthening. Phase transformations are induced through appropriate heat treatments [10]. Other phases, such as borides, are also introduced, although their contributions provide greater effects in creep rate, rupture life, and rupture strain. They do not provide additional strengthening due to the small volume fractions that they represent [11]. GTD-111 is microstructurally more stable than Inconel 738LC and has better mechanical properties which make GTD-111 more reliable for use at high temperatures [12], although microstructural degradation such as MC carbide decomposition, agglomeration of the γ' , and formation of minor phases [13] takes place in either alloy when exposed to high temperatures.

2.1 MICROSTRUCTURE

The GTD-111 superalloy mainly consists of a gamma (γ) matrix. The main secondary phase is the gamma-prime (γ'), which is the principal strengthening phase of nickel and iron-nickel base superalloys. Other phases such as gamma double-prime (γ'') and carbides (MC, $M_{23}C_6$, and M_6C) are present on the GTD-111 superalloy to provide better properties (creep resistance) than the previously used Inconel 738 superalloy.

2.1.1 Gamma Phase (γ)

The gamma matrix (γ) is preferred by most designers, because of its high modulus of elasticity and low diffusivity, which promote the high creep rupture resistance due to the following main reasons: a) nickel shows very low phase instability (its third electron shell is almost filled); b) with chromium additions, nickel forms Cr_2O_3 -rich scales which restricts the diffusion rates of the metallic elements outward, and oxygen, nitrogen, sulfur, and other atmospheric elements inward; and c) at high temperatures nickel forms Al_2O_3 rich scales, which provides great oxidation resistance [14].

The austenitic phase matrix is strengthened by solid-solution elements such as cobalt, iron, chromium, molybdenum, tungsten, titanium, aluminum, and by carbide precipitation. Aluminum not only provides oxidation resistance, but it also helps the formation of γ' phase along with titanium.

Molybdenum, besides acting as a solid-solution strengthener, and tungsten also helps the formation of carbides in the form of $M_{23}C_6$ and M_6C , which help the nickel based superalloy in three main ways: a) provide grain boundary strength when properly formed; b) fine carbides when precipitated in the matrix provide strength; and c) carbides tie up elements that could cause phase instability, such as borides (in high quantities) impairing creep resistance. Chromium, niobium, tantalum, and titanium also helps the formation of carbides such as MC , M_7C_3 , $M_{23}C_6$, and M_6C , which are described in section 2.1.3 in this chapter [15].

2.1.2 Gamma Prime (γ') Phase

It's a geometrical closed pack (GCP) which has an ordered FCC structure. It's spherical in most cases in iron-nickel and nickel based alloys. Size varies with exposure to time and temperature. It's also the principal strengthening phase in nickel and iron-nickel base superalloys. Volume fraction and distribution of γ' are important parameters for control of properties. Adding aluminum and titanium, the volume fraction increases. Optimal strength results when γ' particle size range is 0.01 to 0.05 microns.

2.1.3 Gamma Double Prime (γ'')

The gamma double prime (γ'') phase has an ordered body centered tetragonal (bct) crystal structure and forms in superalloys that are rich in niobium or tantalum. It precipitates as fine coherent platelets in the γ matrix and on γ' particles with a specific orientation $\{100\}$ [16]. It acts as a strengthening phase due to the coherency strains between the γ/γ'' lattice mismatch. The gamma double prime γ'' phase is not a stable phase thus restricting applications to temperatures below 700° C (1290° F). Applications above this temperature produce a loss of strength due to the coarsening of γ'' , and the dissolution between γ'' and γ' [17].

2.1.4 Carbides

Carbon is added to the GTD – 111 alloy at levels of approximately 0.08% to 0.12% and combining with refractory elements such as titanium, tantalum, and hafnium forms the MC carbides. During the alloy's heat treatment and high temperature service exposure, these MC carbides decompose into lower carbides like $M_{23}C_6$ and M_6C , which will eventually segregate into the grain boundaries [18]. Some of the most important carbides in nickel-based superalloys are: MC, M_6C , and $M_{23}C_6$. M is substituted by a metal atom such as chromium, molybdenum, titanium, tantalum, or hafnium. The high-temperature creep properties of the superalloys are improved by carbides and borides.

Carbides provide three functions:

- a) Grain boundary carbides strengthen the grain boundaries,
- b) prevent grain boundary sliding, and
- c) permit stress relaxation.

If fine carbides are precipitated in the matrix, strengthening occurs. They also help tie up elements that could result in phase instability. Carbide precipitation in Nickel based alloys have a tendency to form in grain boundaries. Morphology of carbides can degrade properties such as reducing carbon content, which reduces creep life and ductility. Aging of Nickel-base superalloys causes $M_{23}C_6$ to form at grain boundaries, but if they precipitate continuously (i.e. film formation), properties will be degraded [19].

2.1.4.1 MC Carbides

MC carbides have a random cubic (or irregular), large globular particles, gray to lavender color. They are formed in superalloys shortly before freezing [20]. They are usually substituted by titanium (most common), tantalum, hafnium and niobium (less common). Titanium carbide can have some solubility for nitrogen, zirconium and molybdenum [21]. MC has a cubic crystal structure (FCC) and they are a major source of carbon for chemical interaction later on the superalloy forming process. They are very dense, close packed structures, and very strong.

2.1.4.2 $M_{23}C_6$ Carbides

$M_{23}C_6$ is the most important carbide. It forms at grain boundaries on the γ – phase during aging and when properly formed, it increases strength of the grain boundaries to balance matrix strength.

Chromium is the primary “M” element but iron, molybdenum, or tungsten can substitute it. They have irregular discontinuous blocky particles but sometimes can form as regular geometric forms. They are mostly located in the grain boundaries, but sometimes form along twin boundaries, twin ends, and stacking faults, forming a film structure. They also feature an FCC crystal structure. $M_{23}C_6$ carbides form in alloys that have a moderate to high chromium content. They form from the degeneration of MC carbides and from soluble carbon residual in the γ – phase during the lower temperature heat treatment and service ($\sim 1400^\circ\text{F} - 760^\circ\text{C}$) [22]. Their effect on the superalloys is positive since they increase rupture strength through grain boundary sliding. The downside is that most ruptures start by fracture of the $M_{23}C_6$ carbide boundaries or by decohesion of the $M_{23}C_6$ carbide – γ - phase interface.

2.1.4.3 M_6C Carbides

The M_6C carbide is rich in molybdenum or tungsten, but they can be replaced by chromium, nickel, or cobalt. They form when the molybdenum and/or tungsten content is around 6-8%. This carbide is presented in as-is cast condition distributed in the γ – matrix. It mostly precipitates in the grain boundaries (to control grain size). They usually form at high temperatures $1500\text{-}1800^\circ\text{F}$ ($815^\circ\text{C} - 980^\circ\text{C}$), and has an FCC crystal structure [23]. The temperature at which this carbide forms is higher than the temperature formation of the $M_{23}C_6$ carbide. Figure 2.3 shows the solidification sequence of the GTD-111 alloy.

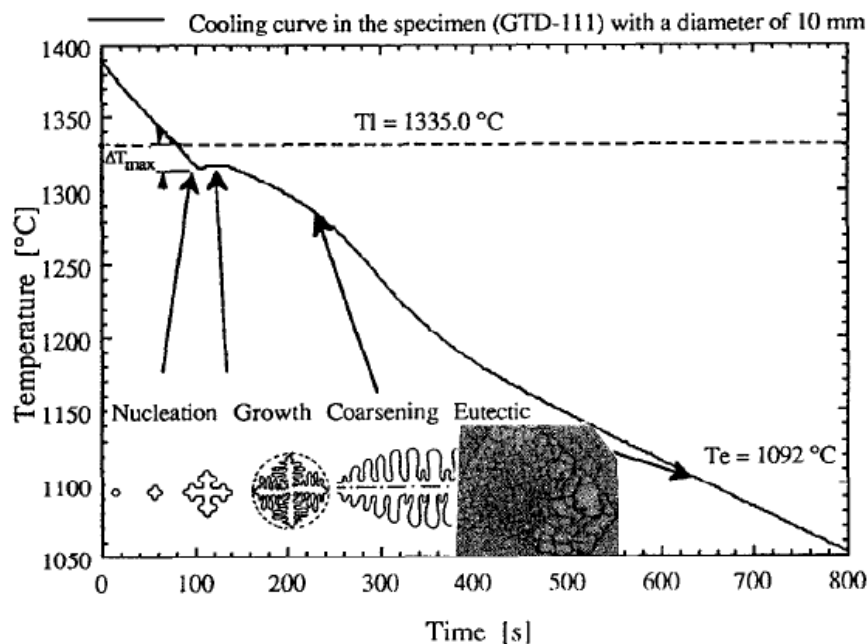


Figure 2.3 – Solidification sequence of GTD-111 superalloy [24].

Chapter 3: Experimental Program

This research was divided into several stages: a) microstructure, b) elemental composition determination using energy dispersive x-ray spectroscopy (EDS), c) microhardness testing, d) gamma-prime (γ') diameter determination using the scanning electron microscope (SEM), and e) transmission electron microscopy (TEM). All of these tests were conducted using a General Electric Frame 3/2 Model “J” Dry Low NO_x Unit (1st stage buckets). The buckets had been in service for 48, 064 hours but were removed because of a failure of the 2nd stage variable nozzles due to damage caused by a foreign object. The buckets were exposed to an approximate service temperature of 1700 – 1800 °F. Two sections of the buckets were chosen for this experiment: a) airfoil and b) shank. The airfoil section simulated the sample in service since it is the area that is thermally exposed the most; and the shank simulated the new material due to the much less thermal exposure in this section.

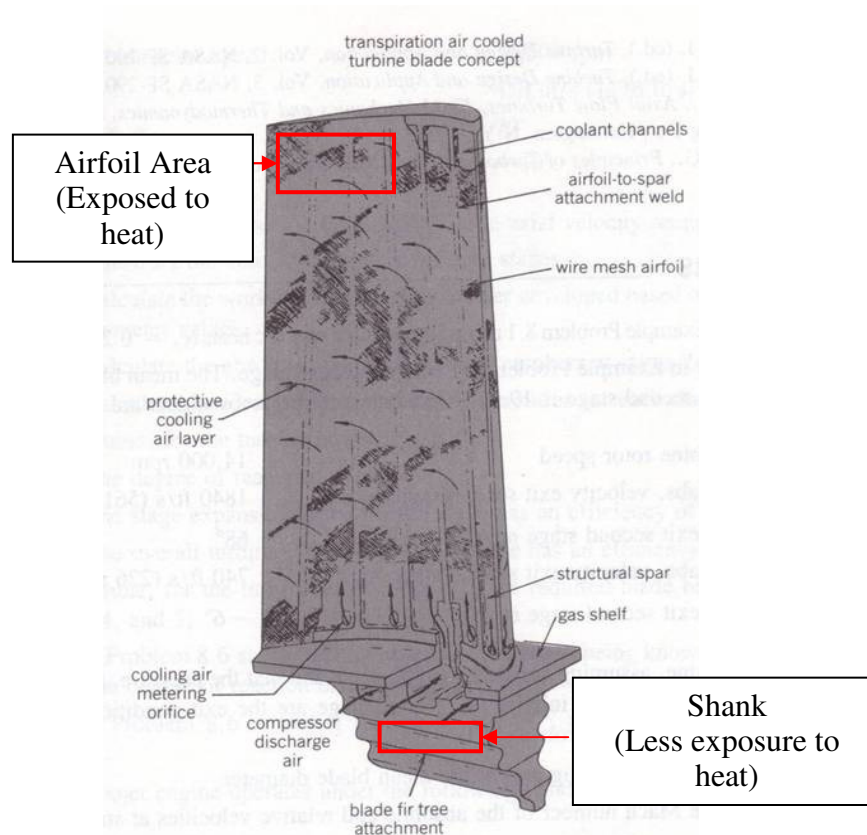


Figure 3.1 – Components of a gas turbine bucket. Red squares show areas used for experiment [25]



Figure 3.2 – Bucket used for this study.

3.1 SAMPLE PREPARATION

Two areas of the turbine bucket were considered for analysis: the airfoil and the shank. The airfoil area of the turbine bucket acted as the used sample (thermally exposed) and the tree attachment (shank) acted as the new sample since it is not completely thermally exposed such as the airfoil itself. Both samples were cut such that the sectioned parts could be used for micro-structural analysis, transmission electron microscopy, elemental composition, scanning electron microscopy, and microhardness analyses.

3.2 MICROSTRUCTURAL ANALYSIS

The shank sample and the airfoil sample were mounted in conductive epoxy resin. The samples were ground with grit paper sizes 60, 120, 180, 240, 320, 400, 600, 800, and 1200. The samples were then polished with the polishing cloth and alumina suspension sizes 5.0 μm , 1.0 μm , 0.3 μm , and 0.05 μm .

The microstructures of shank sample and the airfoil were obtained using Marble's reagent, which consists of 10 g of copper sulfate (CuSO_4) mixed with 50 ml of hydrochloric acid (HCl) and 50 ml of water (H_2O). The samples were etched for approximately 20 seconds.

The microstructures were obtained using the Nikon Epiphot 300 Metallographic Microscope and the images were acquired using the Clemex Vision PE Acquisition Software.

3.3 ELEMENTAL PHASE COMPOSITION DETERMINATION

The elemental composition of the analyzed samples was taken using an INCA X-Act Detector by Oxford Instruments by energy dispersive x-ray spectroscopy (EDS) using a JEOL JSM 6490LV Scanning Electron Microscope (SEM). Since the samples were mounted in conductive epoxy resin, there was no need of sputtering the sample with gold or to cover the samples with carbon tape. EDS was performed on several areas of the samples such as grain boundaries, phases, eutectoid phases, and matrix. The EDS Parameters were 10 mm Working Distance (WD), 15 kilo-Electron Volts (KeV), and at High Vacuum (HV). Results obtained by EDS are qualitative results.

3.4 HARDNESS

The hardness testing was performed using a Future Tech Microhardness FM Tester and the Clemex CMT Acquisition Software. A microhardness test profile was performed on one area of the new sample and on three areas of the used sample.

3.5 GAMMA PRIME (γ') DIAMETER

The gamma prime (γ') diameter was measured using the JEOL JSM 6490LV Scanning Electron Microscope (SEM).

3.6 TRANSMISSION ELECTRON MICROSCOPY (TEM)

Two parts of the gas turbine bucket were sectioned: one from the airfoil and one from the shank area. Each piece was mounted in Multifast Epoxy Resin and grounded until a thickness of less than 0.2 mm was achieved. Once the desired thickness was achieved, the samples were inserted into the TEM sample punch disc tool. Finally the samples were electropolished using the Struer TenuPol Jet Polisher with an etchant solution consisting of 90% methanol, and 10% Perchloric Acid (HClO_4) at a temperature of -30°C and 20 V [26].

After etching, transmission electron microscopy (TEM) was performed using the Hitachi H-8000 Analytical Transmission Electron Microscope and the pictures were developed using the following

procedure: the film negative was immersed using the Kodak Developer D-19 for 4 minutes, then washed with running water for 1.5 minutes. Afterwards, negatives were exposed with Kodak Professional Fixer for 7 minutes, then washed with running water for 30 minutes, and finally immersed with Kodak Photo-Flo 200 Solution for 20 seconds. Finally the images were scanned using the Canon Canoscan 656U Scanner.

Chapter 4: Results

4.1 MICROSTRUCTURAL ANALYSIS

4.1.1 Airfoil (trailing edge)

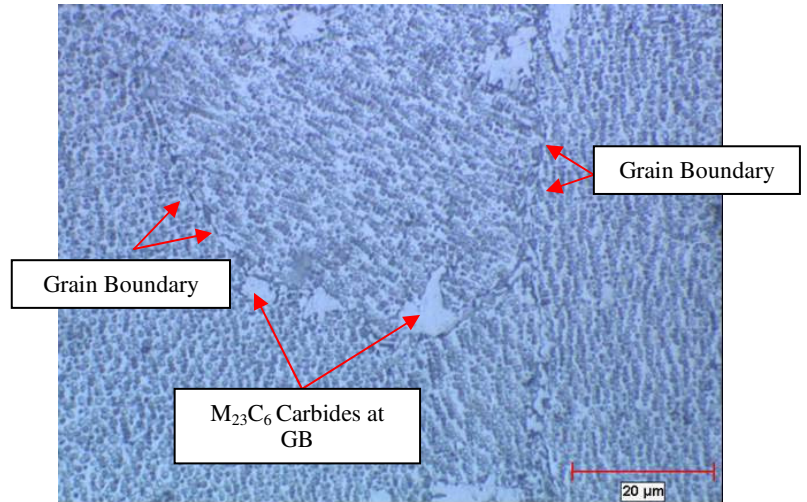
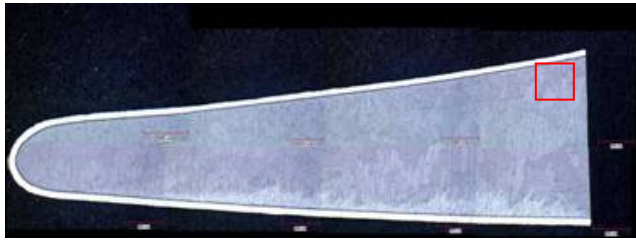


Figure 4.1 – $M_{23}C_6$ carbides were found along the grain boundaries.

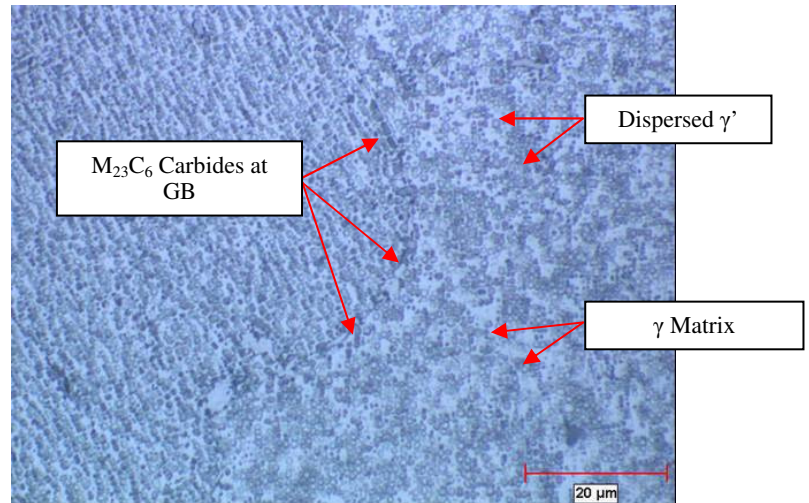
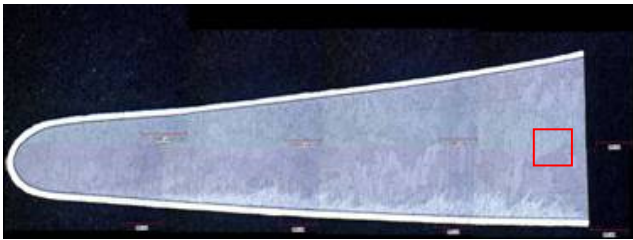


Figure 4.2 – $M_{23}C_6$ carbides were found along the grain boundaries. Dispersed γ' was found along the γ matrix.

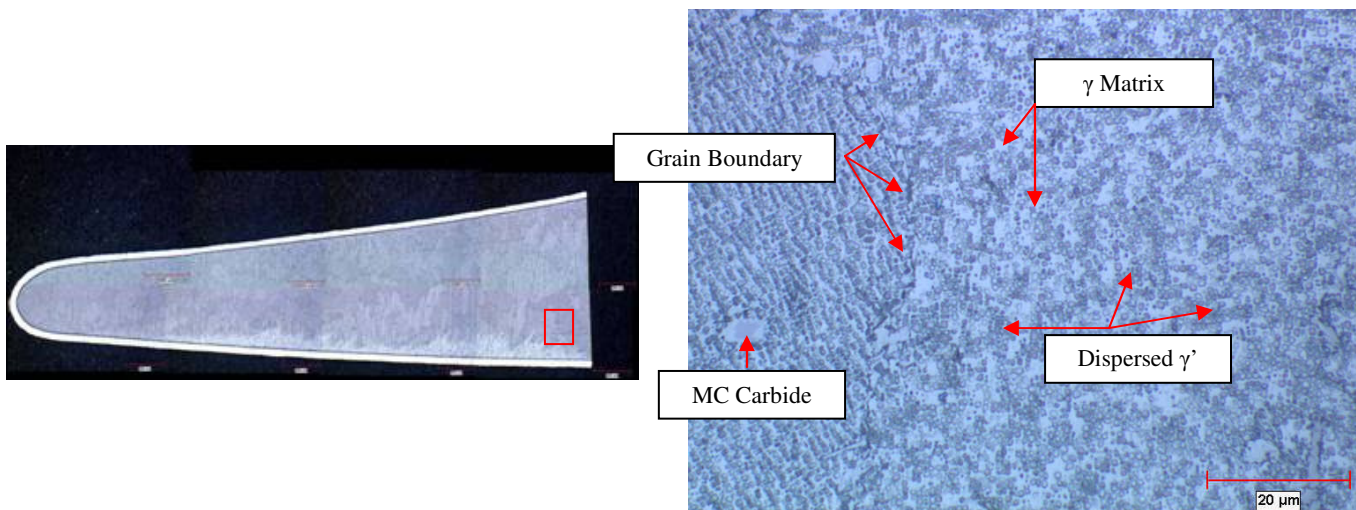


Figure 4.3 – Dispersed γ' was found along the γ matrix. γ' islands are present in some areas of the γ matrix along the grain boundary.

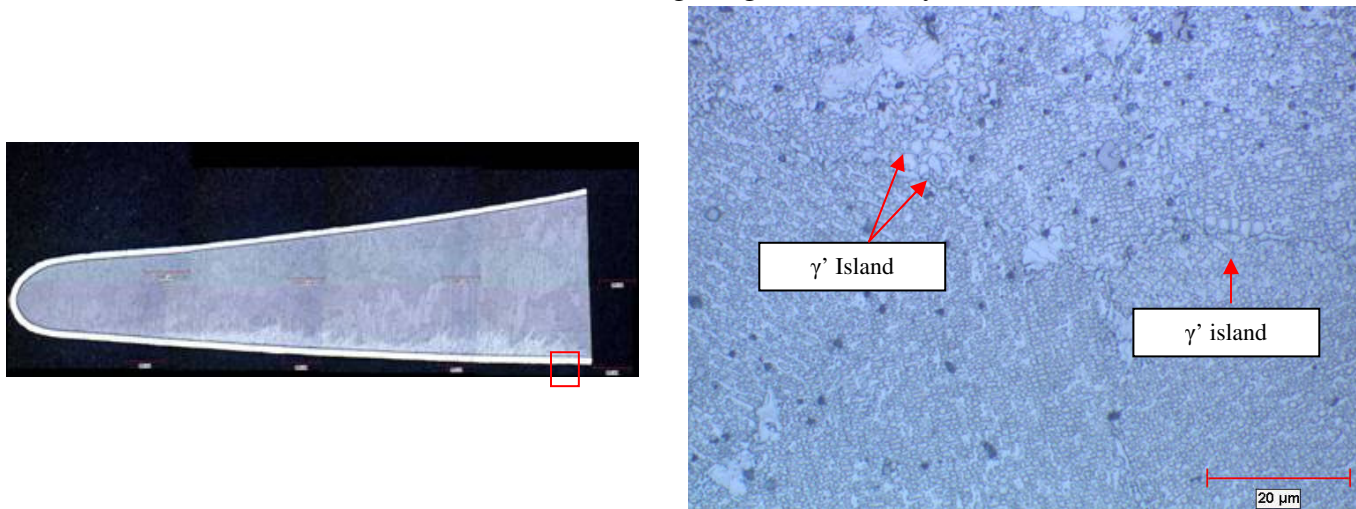


Figure 4.4 - γ' islands dispersed was found along γ matrix. γ' islands are also present on the grain boundary.

4.1.2 Shank

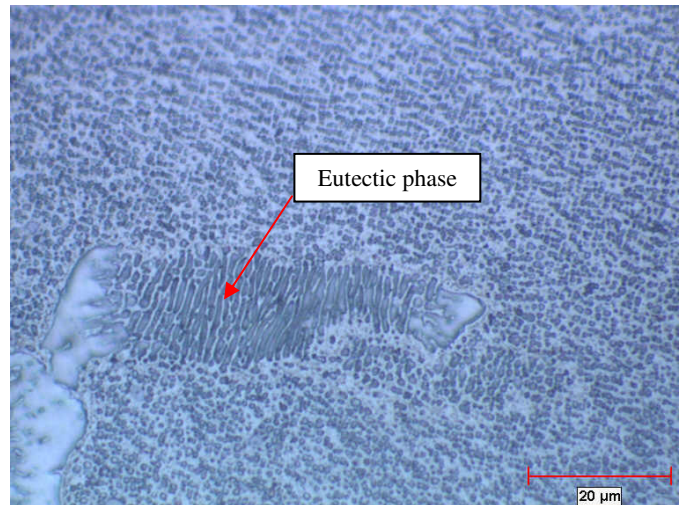
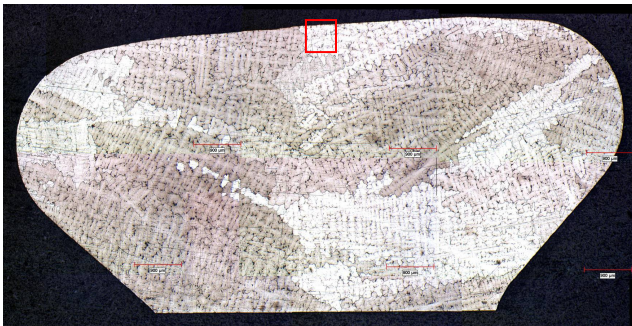


Figure 4.5 – Eutectic phase.

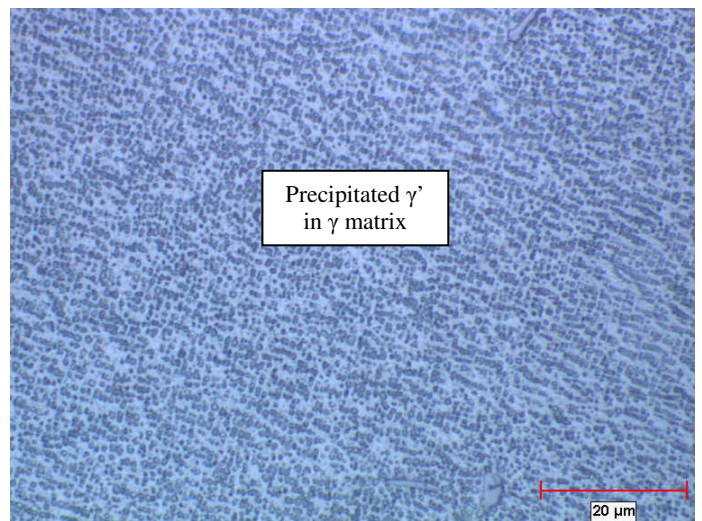
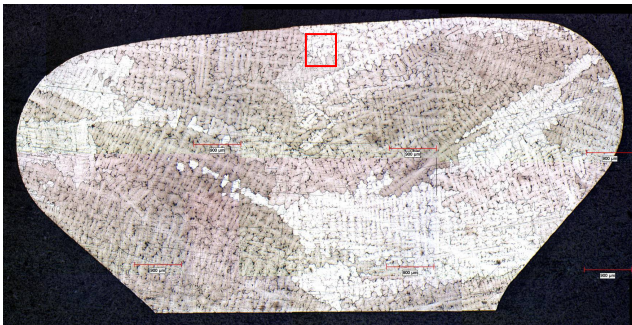


Figure 4.6 – Dispersed γ' was found along the γ matrix.

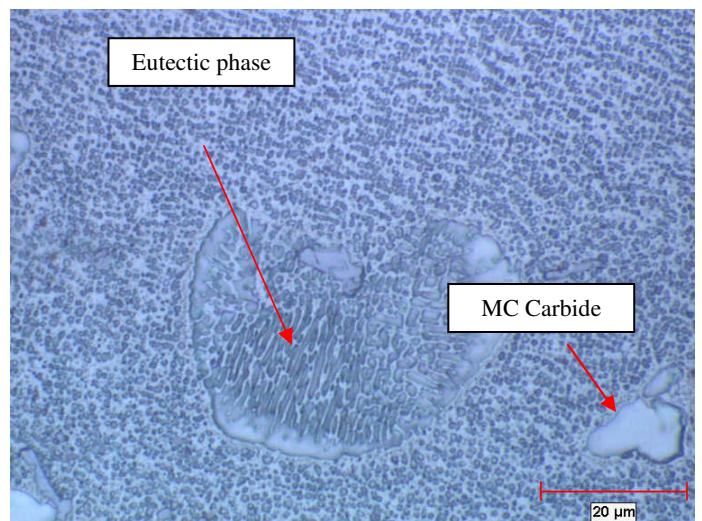
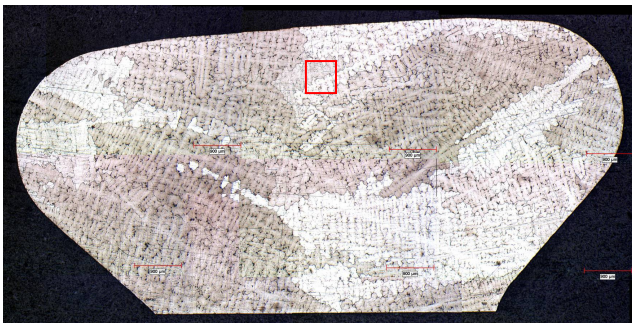


Figure 4.7 – Eutectic phase and MC carbide islands were found in γ matrix.

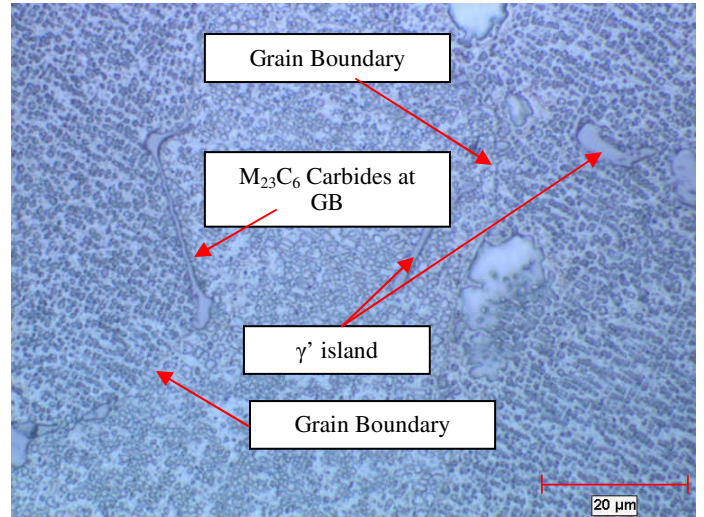


Figure 4.8 – $M_{23}C_6$ carbides were found the grain boundaries. γ' islands were present in the γ matrix and on the grain boundaries as well.

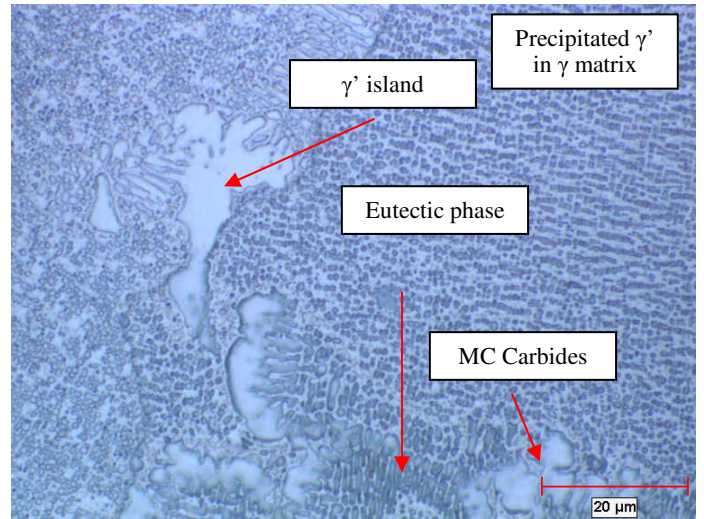
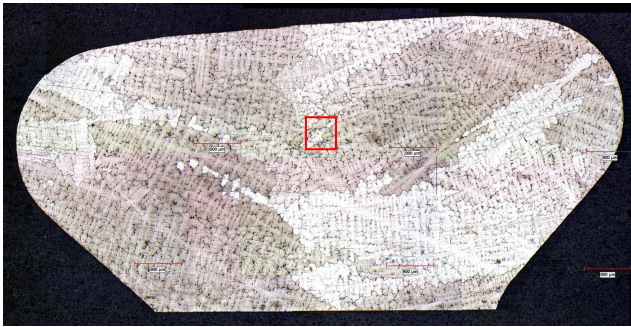


Figure 4.9 - γ' island located at grain boundary. Dispersed γ' is also present on the γ matrix. Eutectic phases and γ' islands were also found in the matrix. MC carbides are also precipitated in γ matrix.

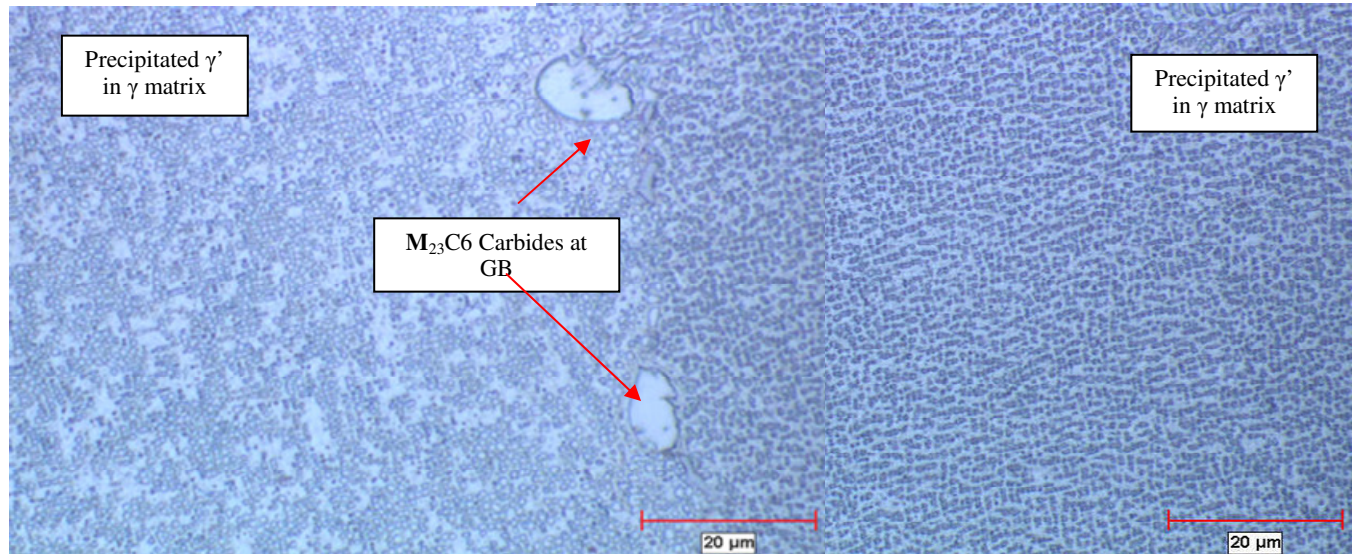
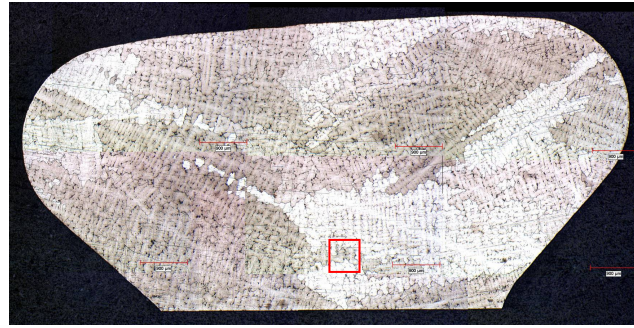


Figure 4.10 – Dispersed γ' in γ matrix. M_{23}C_6 carbides were also present along grain boundary.

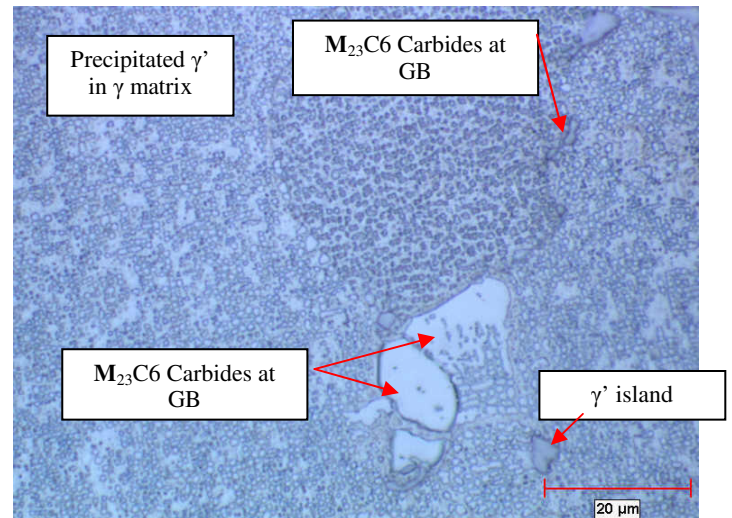
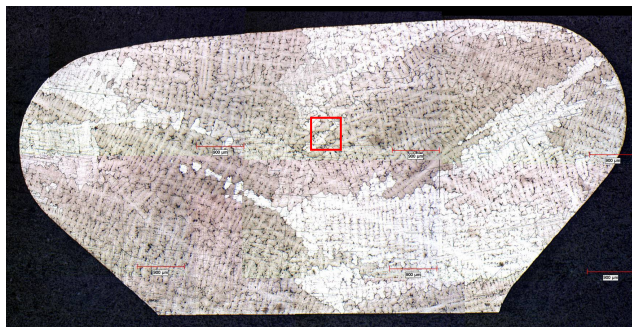
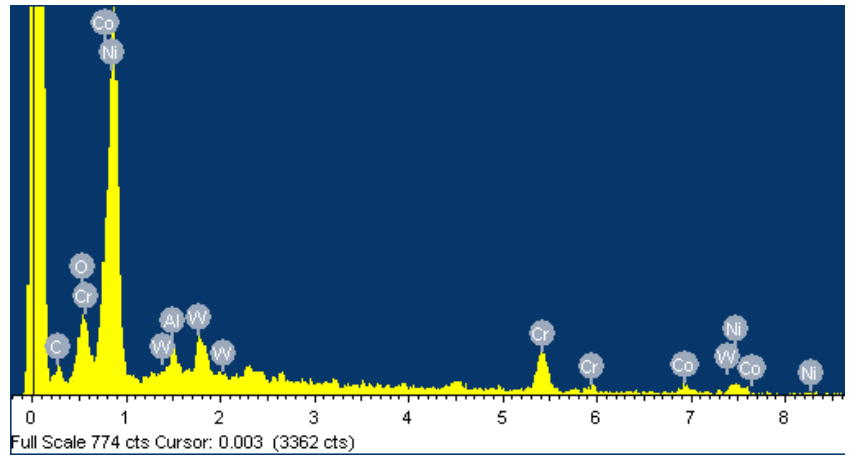
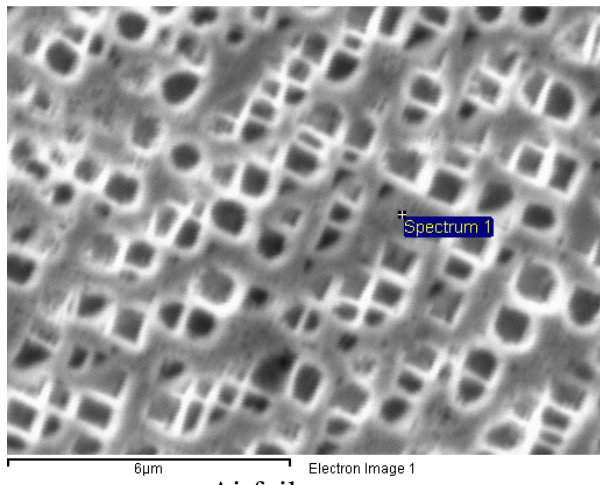


Figure 4.11 – Dispersed γ' is present on the γ matrix. M_{23}C_6 Carbides and γ' islands were also present in the grain boundaries.

4.2 PHASE ELEMENTAL COMPOSITION (EDS) RESULTS

4.2.1 Gamma (γ) Matrix Comparison

Shank



Airfoil

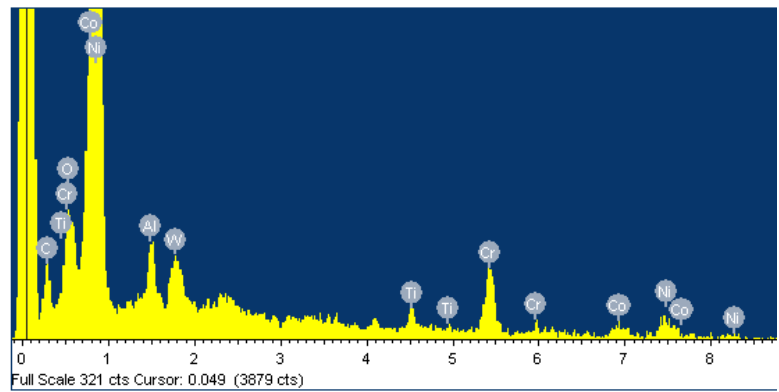
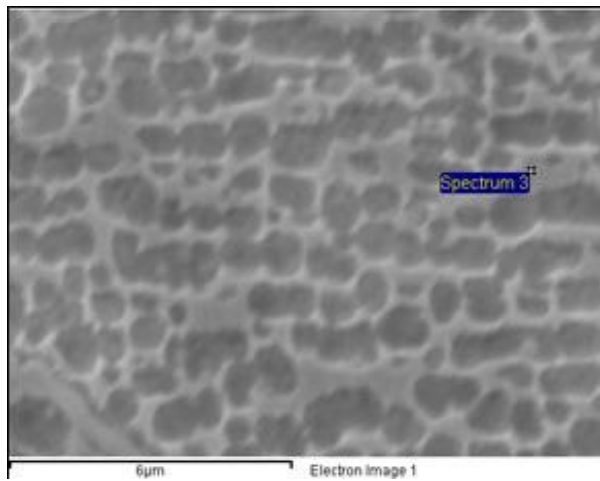
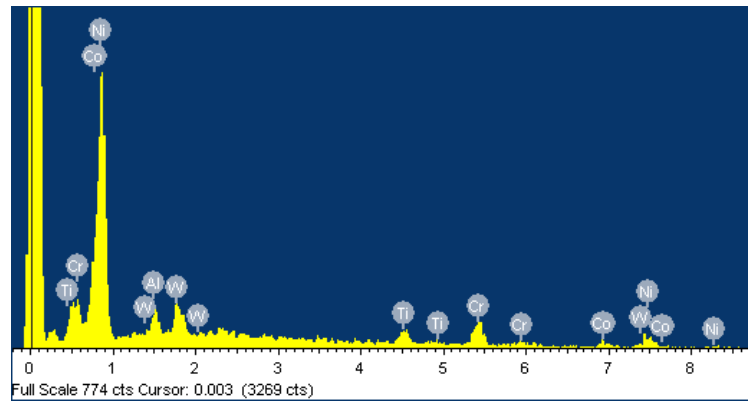
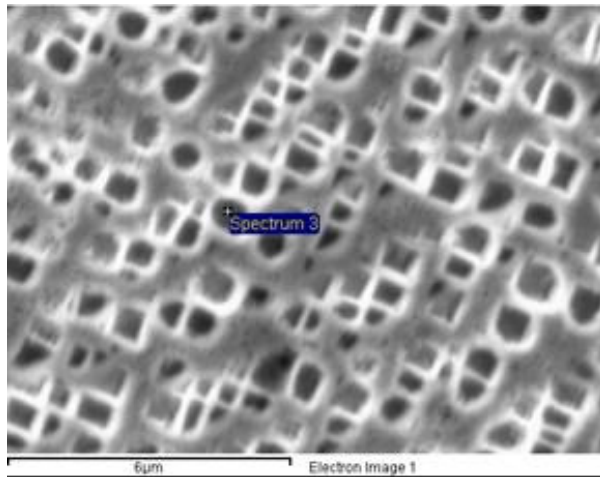


Figure 4.12 – γ matrix qualitative chemical composition. Notice the higher presence of chromium (Cr), aluminum (Al), titanium (Ti) and tungsten (W) in the airfoil sample.

4.2.2 Gamma Prime (γ') Comparison

Shank



Airfoil

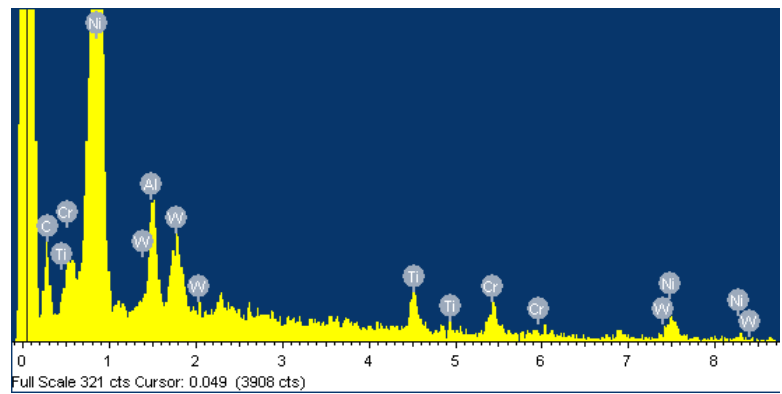
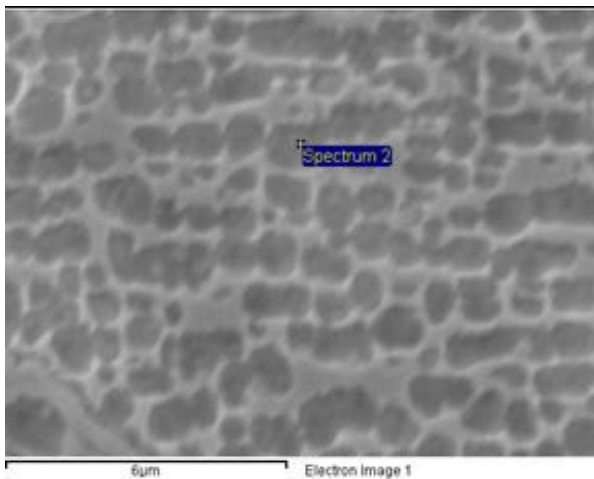


Figure 4.13 – γ' qualitative chemical composition. Notice the higher presence of aluminum (Al), tungsten (W), and titanium (Ti) in the airfoil sample.

4.2.3 MC Carbide Comparison

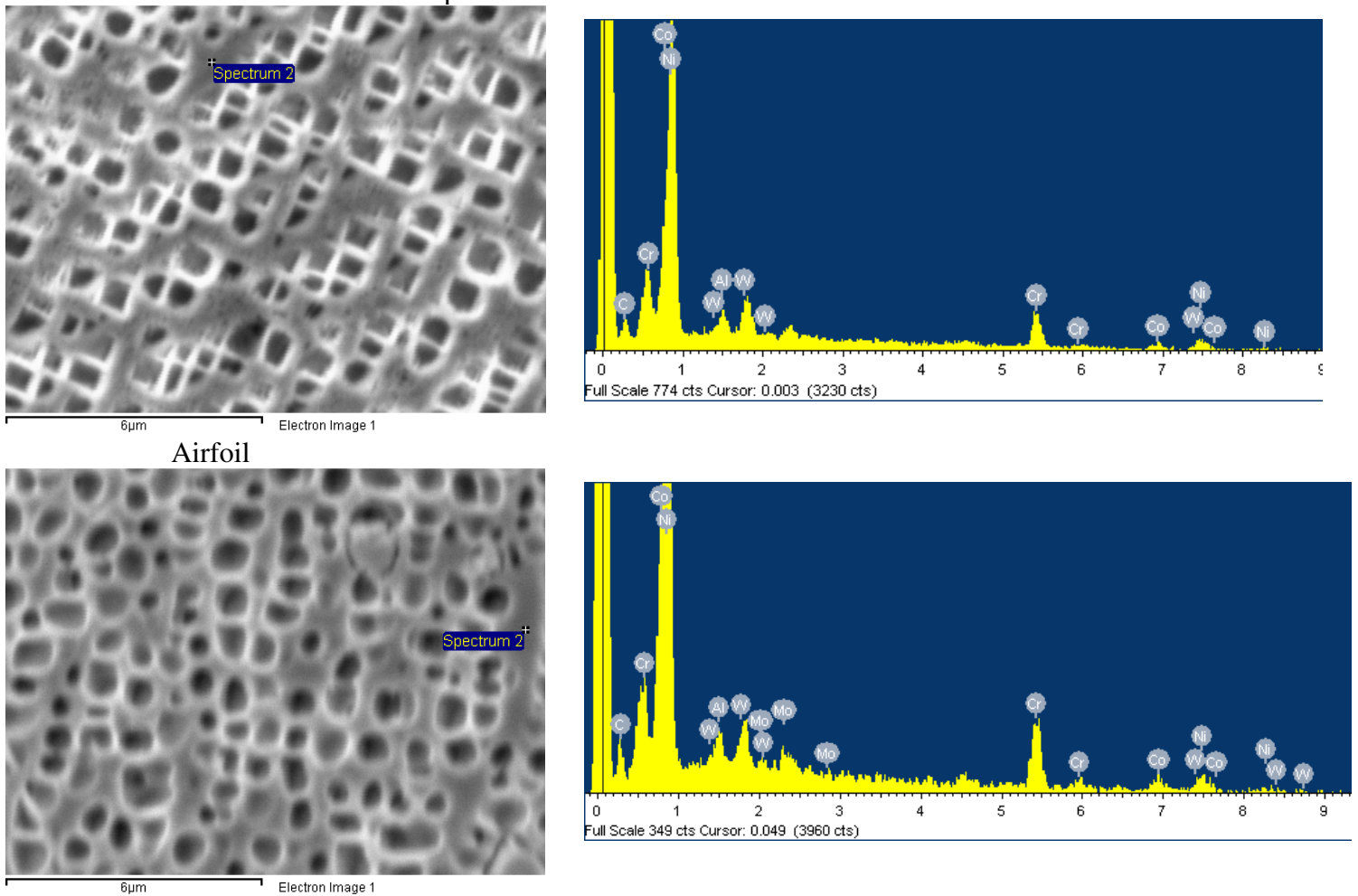
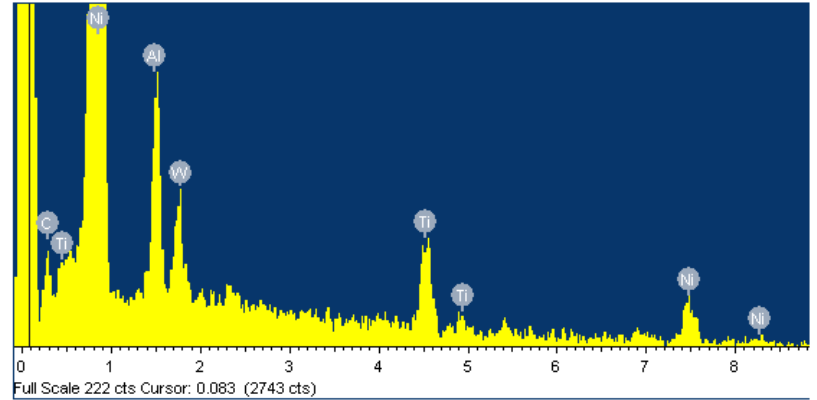
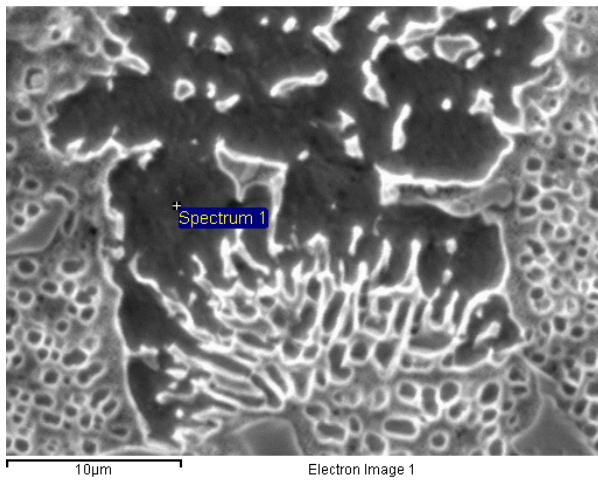


Figure 4.14 – MC carbide qualitative chemical composition. Notice a higher presence of chromium (Cr) in the airfoil sample.

4.2.4 Eutectic Phase Comparison

Shank



Airfoil

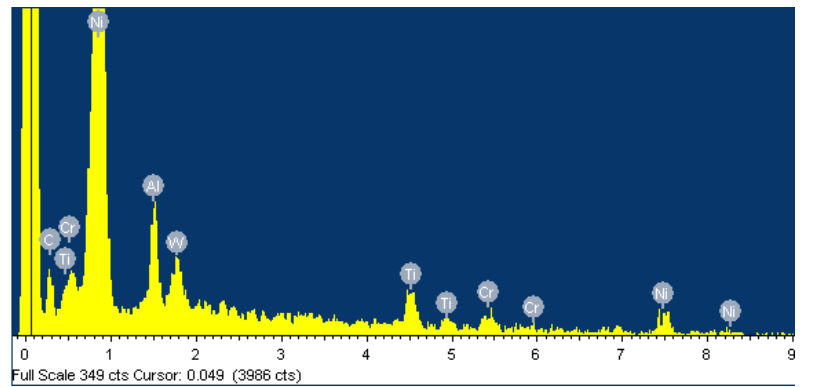
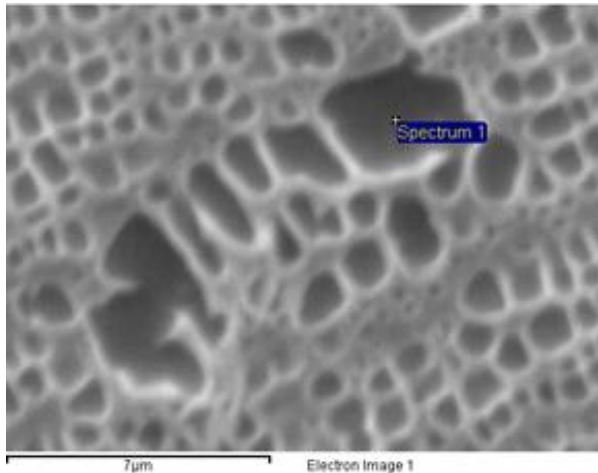
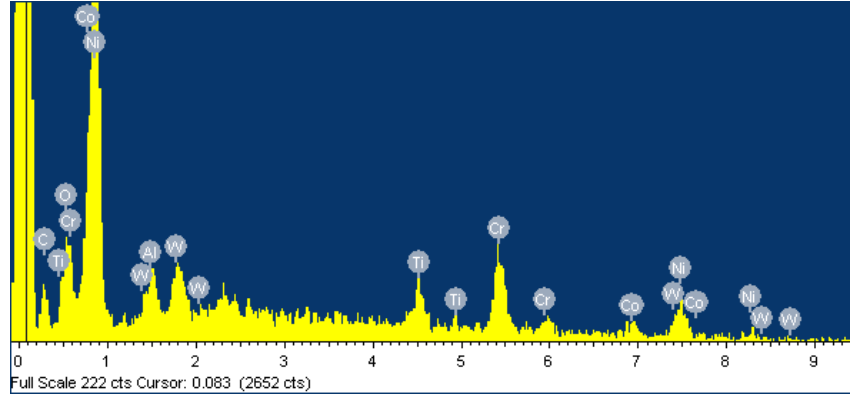
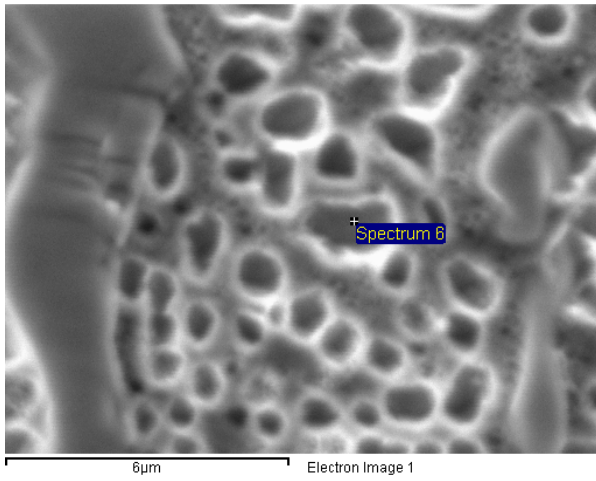


Figure 4.15 – Eutectic phase qualitative chemical composition. Notice a lower presence of titanium (Ti), aluminum (Al), and tungsten (W) in the airfoil sample.

Shank



Airfoil

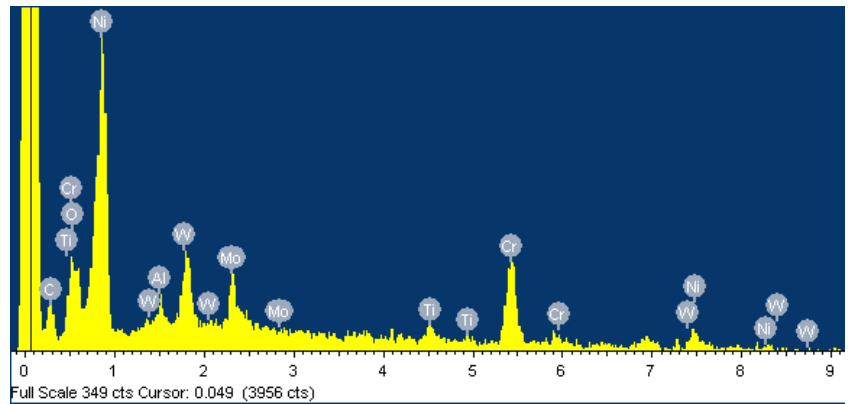
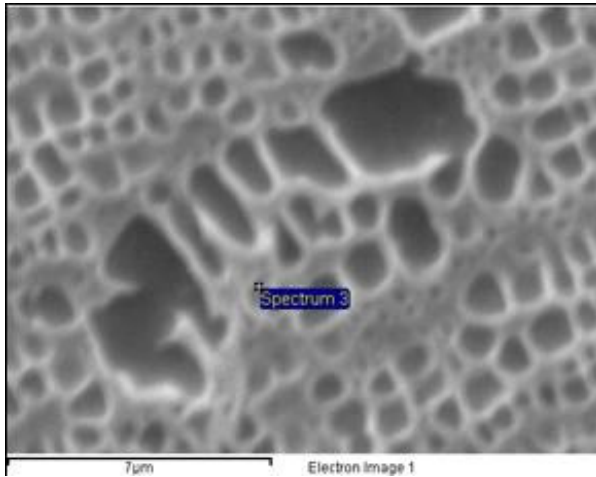


Figure 4.16 – Eutectic phase qualitative chemical composition. Notice a lower presence of aluminum (Al) and titanium (Ti) in the airfoil sample. Shank sample shows a higher presence of tungsten (W).

4.3 HARDNESS RESULTS

4.3.1 Hardness Results for Shank

The hardness results are shown below in Figure 4.41.

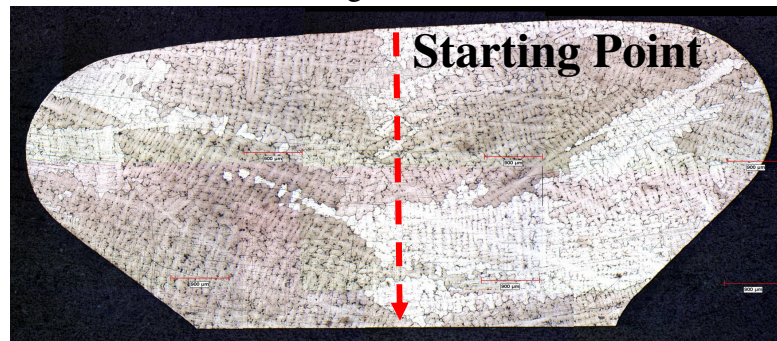


Figure 4.17 – Shank hardness profile cross section

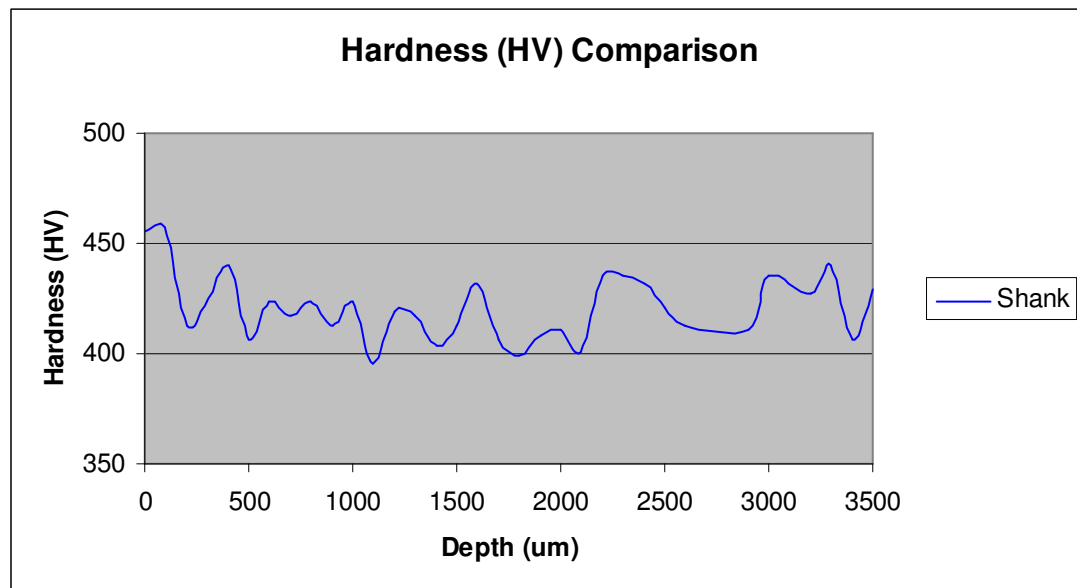


Figure 4.18 – Shank hardness profile results. The results above portray the alloy's hardness as in new condition due to the lack of heat exposure during service.

4.3.2 Hardness Results for Airfoil

The hardness results are shown below in Figure 4.19. The microhardness profile was taken at three different areas because of the differences in thermal exposure due to the bucket's geometry (the trailing edge being thinner (Area 1) than further into the blade (Area 3)).

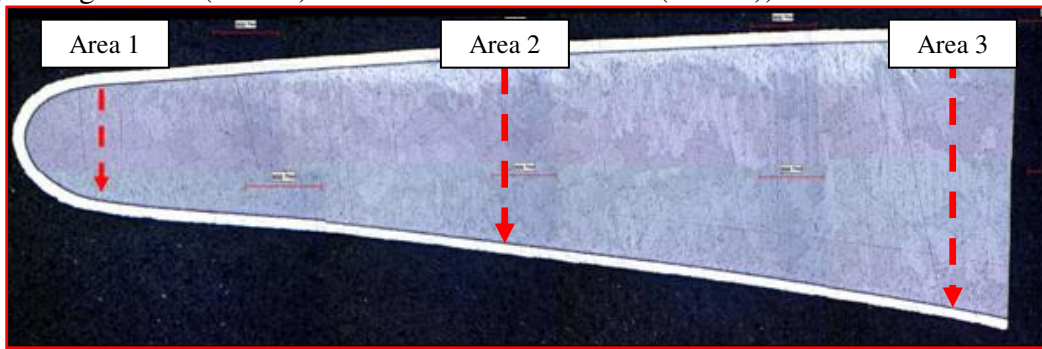


Figure 4.19 - Airfoil microhardness profile cross sectional for Area 1, Area 2, and Area 3.

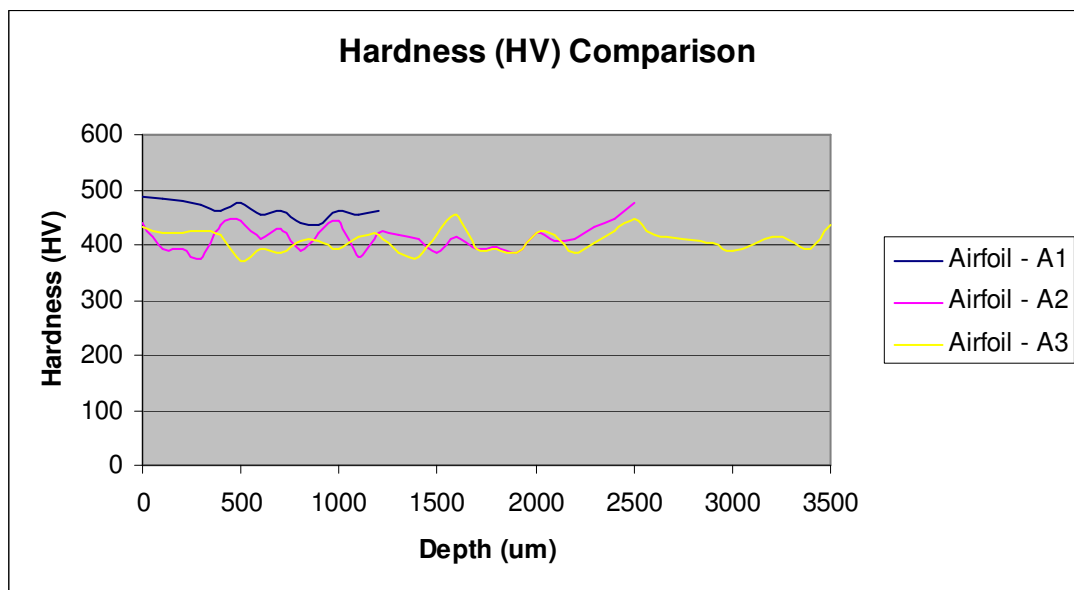


Figure 4.20 – Airfoil hardness profile results for Area 1, Area 2 and Area 3. Areas 2 and 3 have similar hardness results while Area 1 was the area that showed a hardness difference between the analyzed areas.

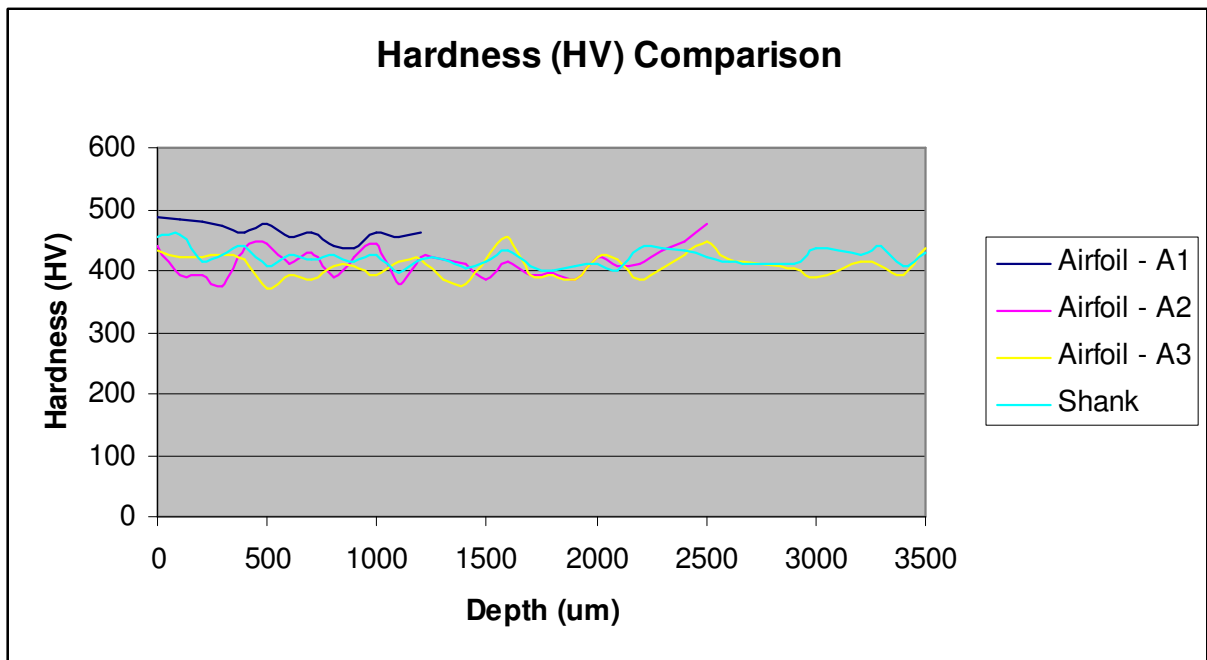


Figure 4.21 – Hardness (HV) comparison between shank and the three areas that were measured in the airfoil. The Area 1 of the airfoil showed a higher hardness than the shank and the rest of the airfoil's areas.

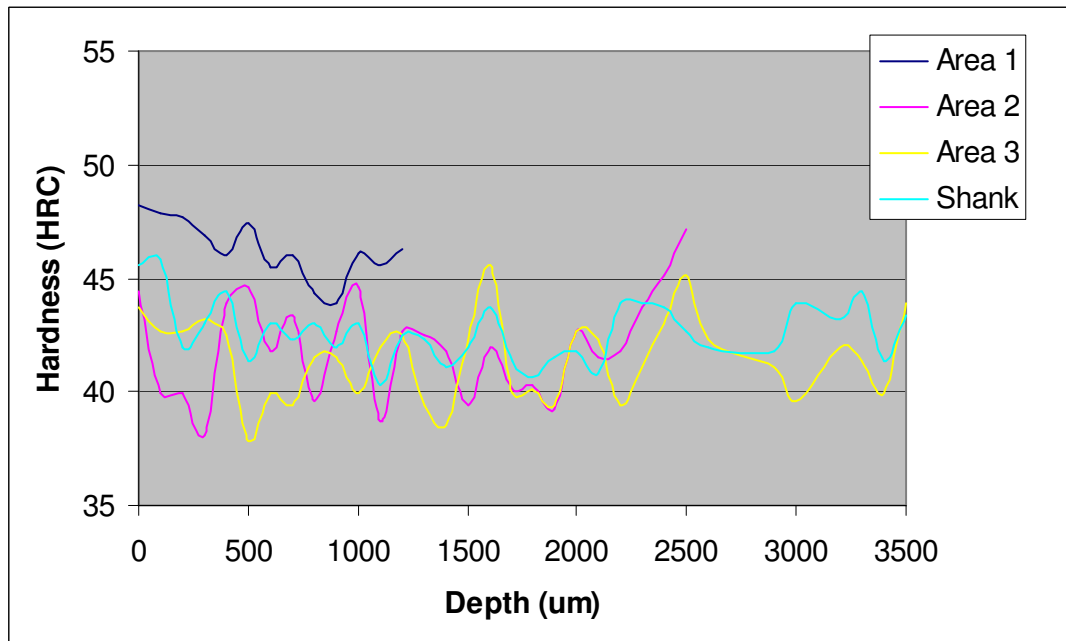


Figure 4.22 – Rockwell hardness equivalent comparison between airfoil and shank

4.4 GAMMA PRIME (γ') DIAMETER

4.4.1 Shank

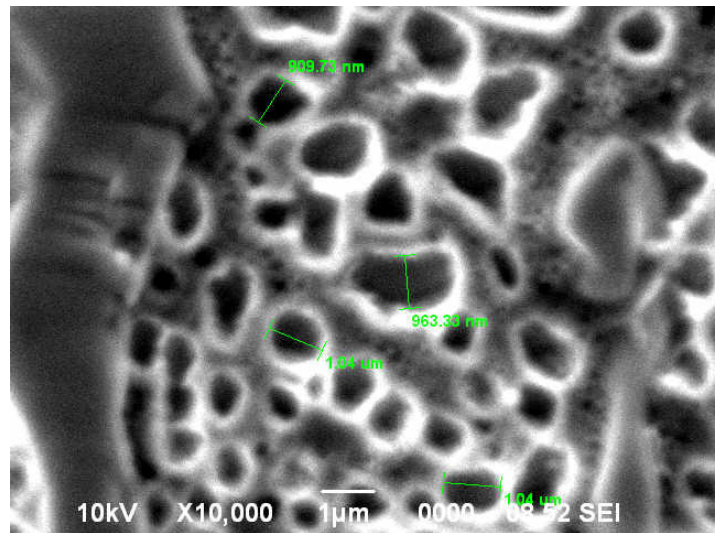
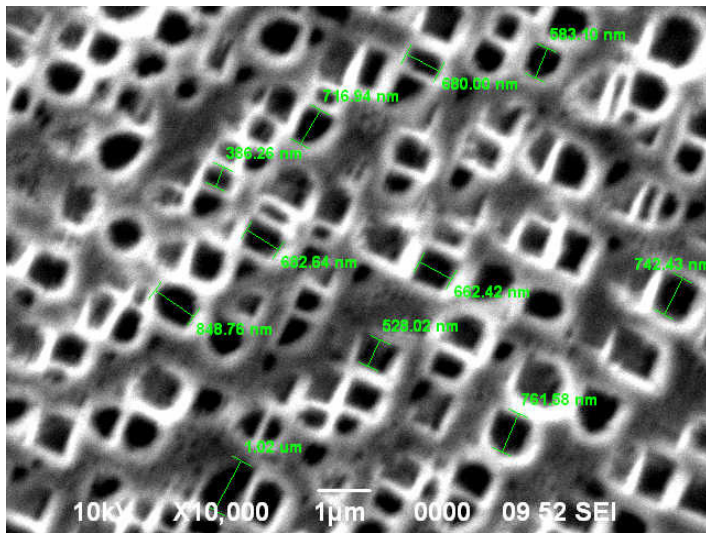


Figure 4.23 – Gamma prime (γ') diameter in shank. See Figure 4.45 for comparison.

4.4.2 Airfoil

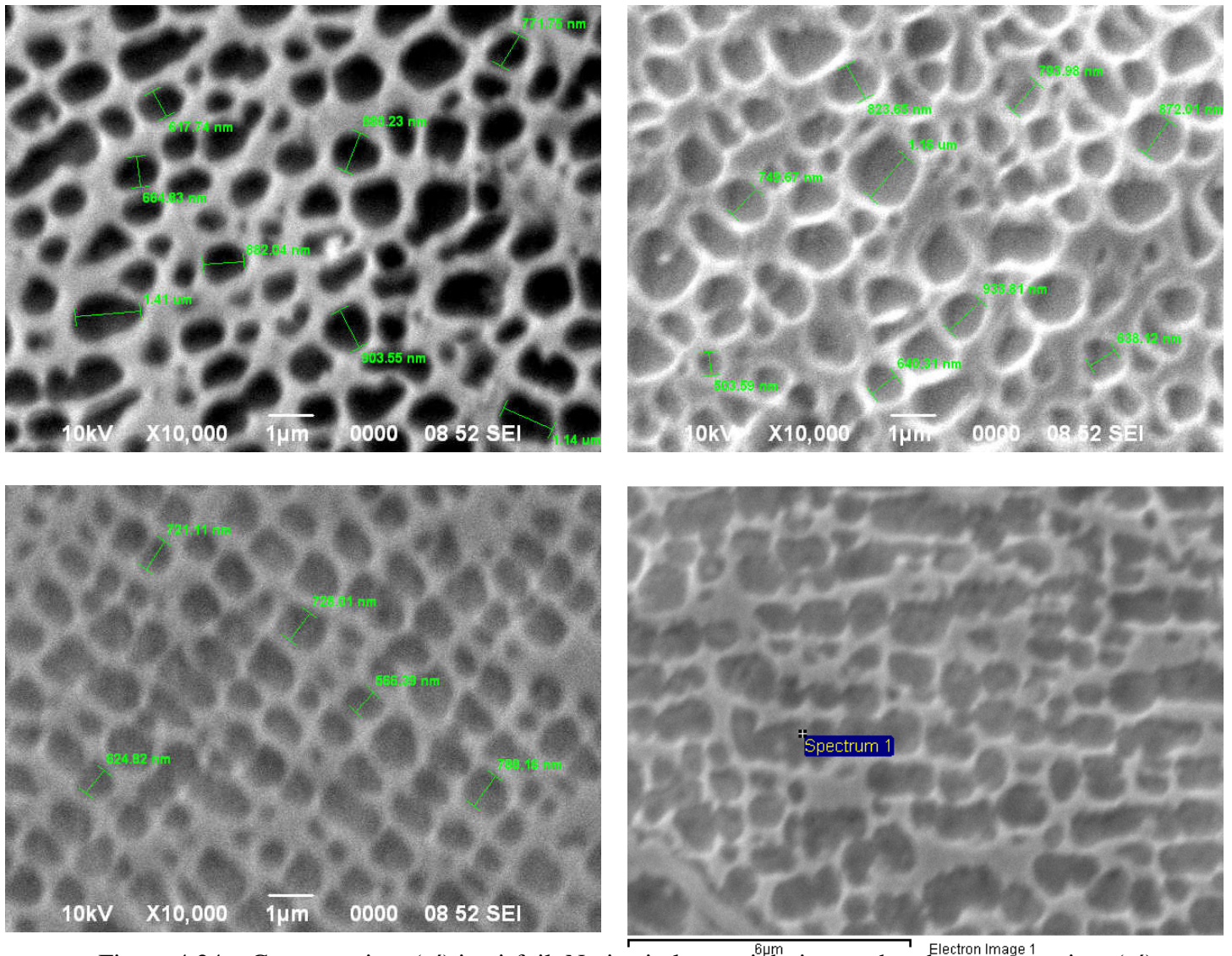


Figure 4.24 – Gamma prime (γ') in airfoil. Notice in lower right image that the gamma prime (γ') coarsens and joins other gamma prime (γ') phases creating a film formation, which weakens the alloy. See Figure 4.45 for comparison.

4.4.3 Gamma prime (γ') Diameter Comparison

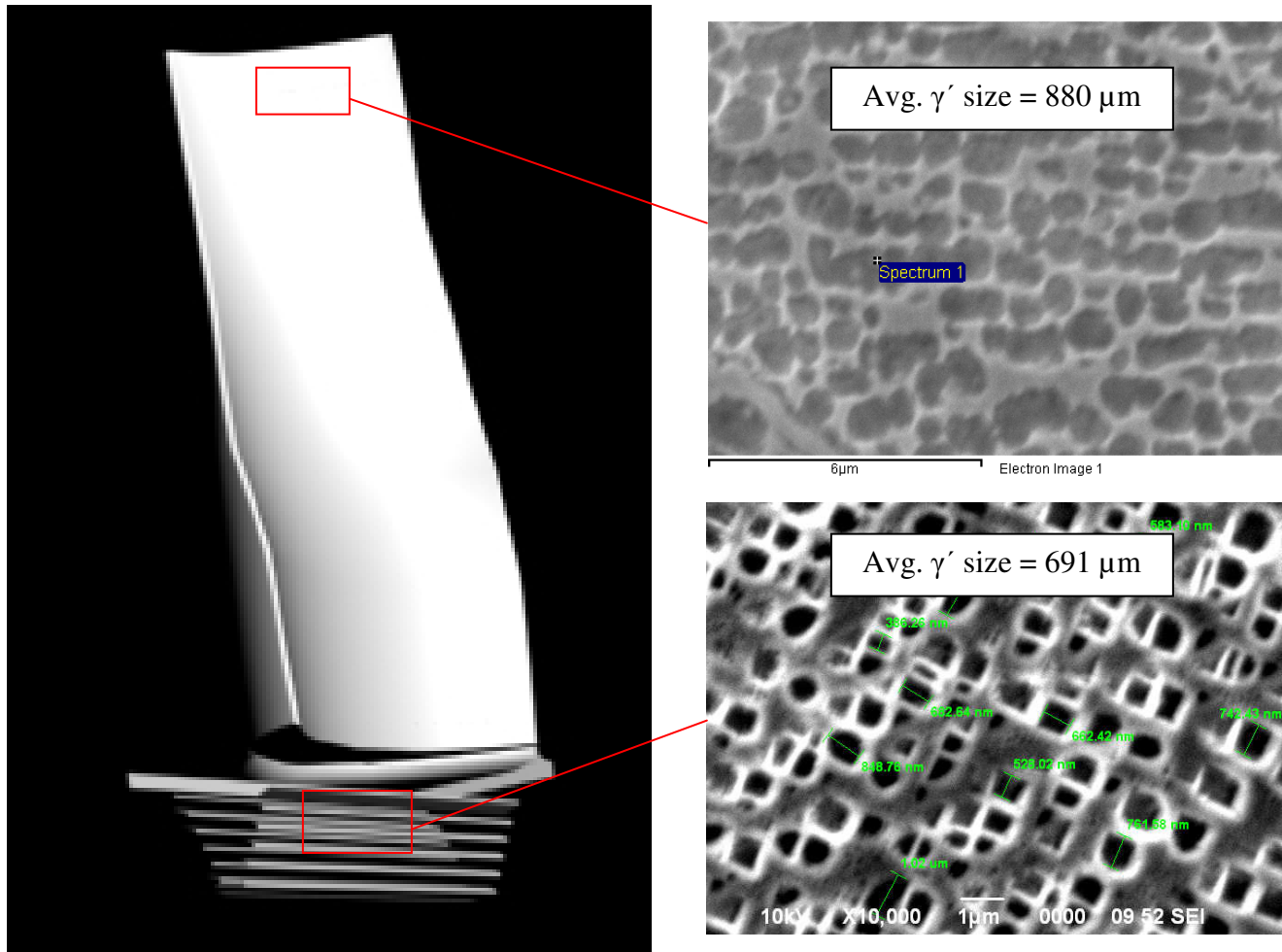


Figure 4.25 - Gamma prime (γ') diameter comparison. Airfoil sample features a larger gamma prime (γ') diameter than the shank sample, which confirms that the gamma prime (γ') of the airfoil gets coarser (compared to the shanks) after exposure to high temperatures. This also confirms that the airfoil's gamma prime (γ') gets coarser at a faster rate.

4.5 TRANSMISSION ELECTRON MICROSCOPY (TEM)

Shank (New)

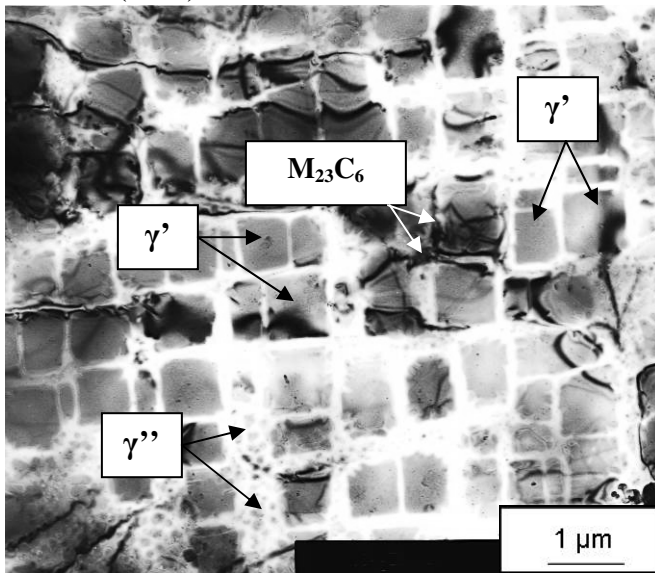


Figure 4.26 – TEM micrograph of shank sample. Notice cuboidal γ' and dispersed γ'' in γ matrix. Electron diffraction pattern for γ' (FCC). $B = [001]$.

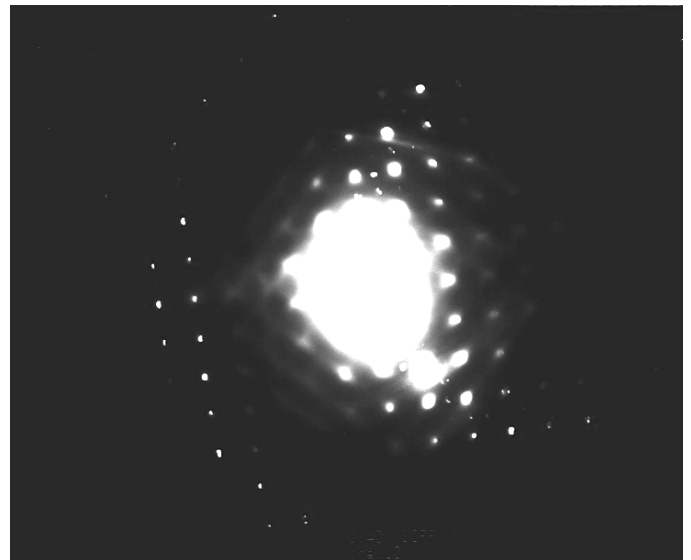
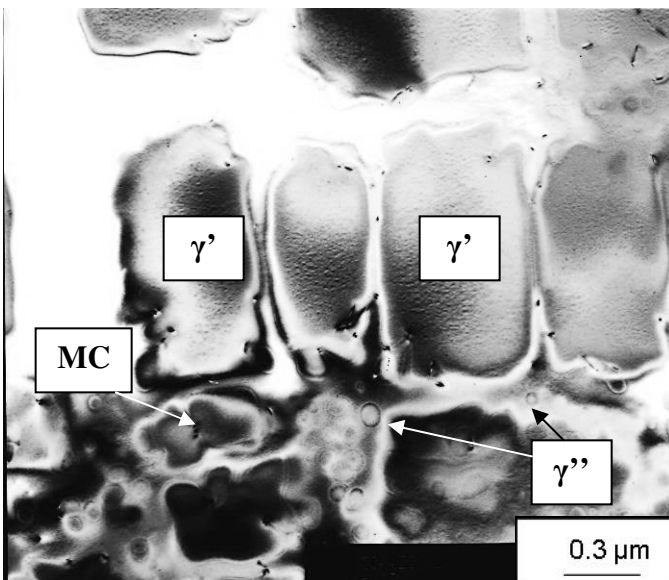


Figure 4.27 - TEM micrograph of shank sample. Notice cuboidal γ' and dispersed γ'' in γ matrix along with an MC carbide island. Electron diffraction pattern for γ' (FCC). $B = [001]$

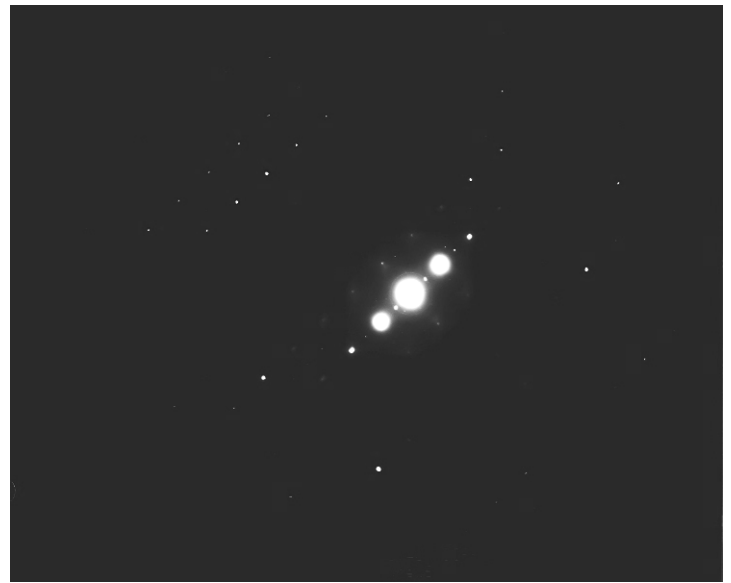
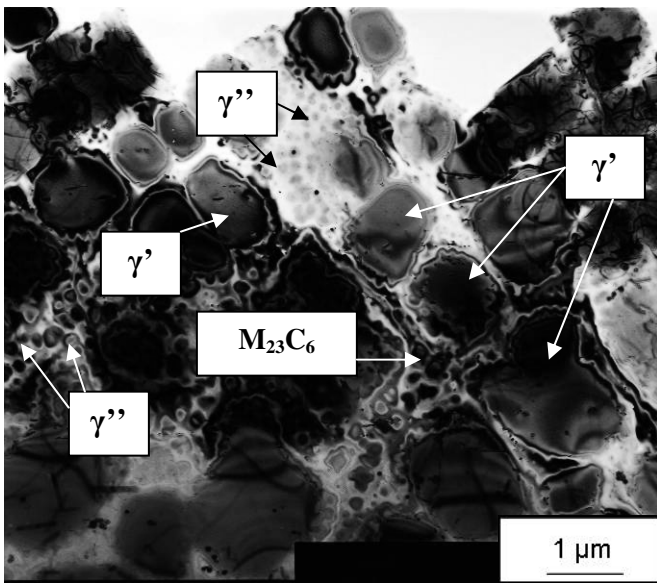


Figure 4.28 - TEM micrograph of shank sample. Notice cuboidal γ' and dispersed γ'' in γ matrix along with an $M_{23}C_6$ carbide. Electron diffraction pattern. $B = [001]$

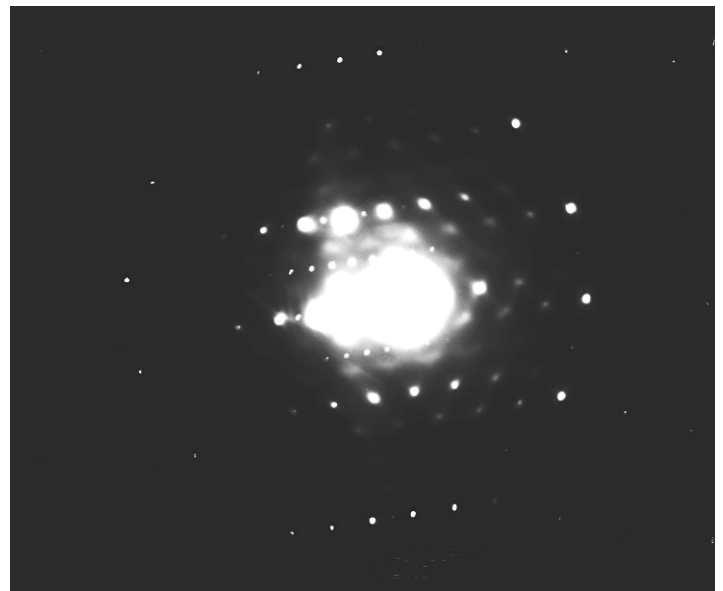
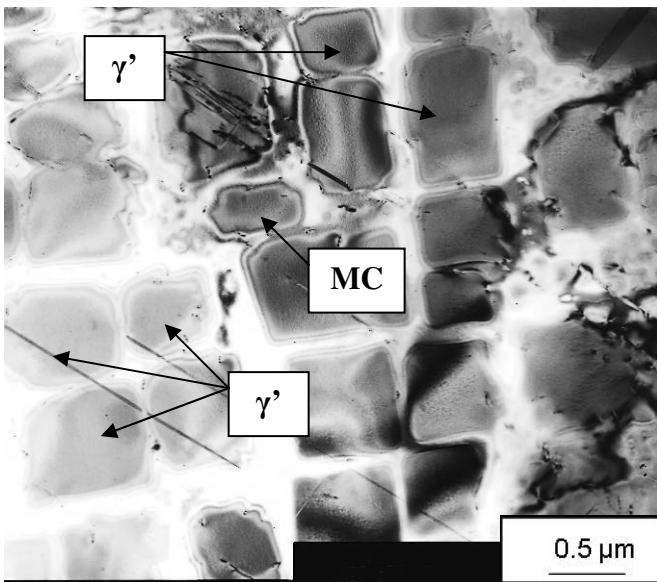


Figure 4.29 - TEM micrograph of shank sample. Notice cuboidal γ' and dispersed γ'' in γ matrix along with an MC carbide island. Electron diffraction pattern for γ' (FCC). $B = [110]$ special reflection.

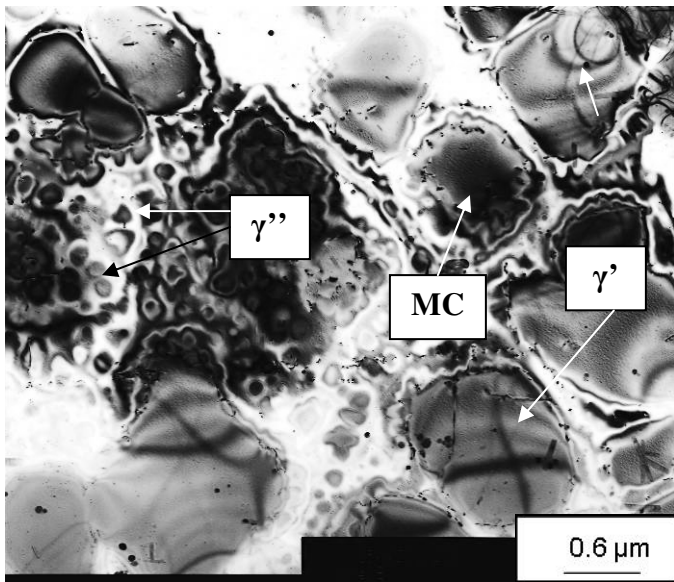


Figure 4.30 - TEM micrograph of shank sample. Notice cuboidal γ' and dispersed γ'' in γ matrix along with an MC carbide island. Electron diffraction pattern for MC carbide (cubic) and γ'' (bct). B = [001]

Airfoil (used)

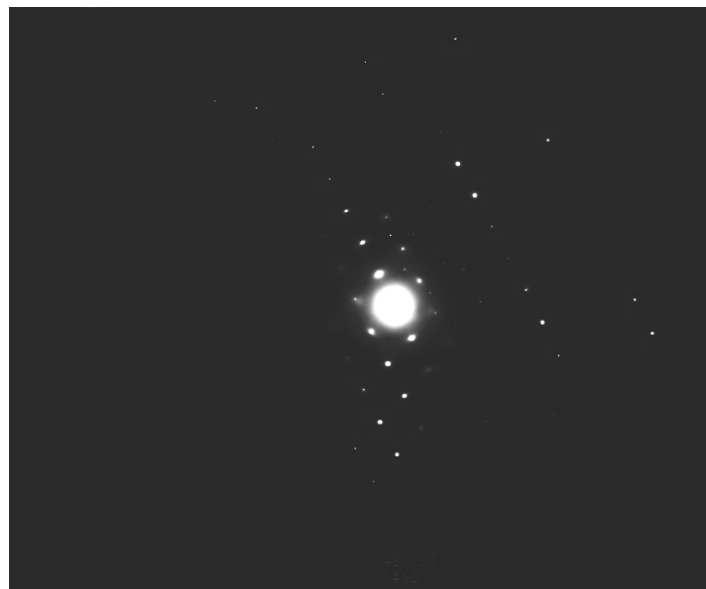
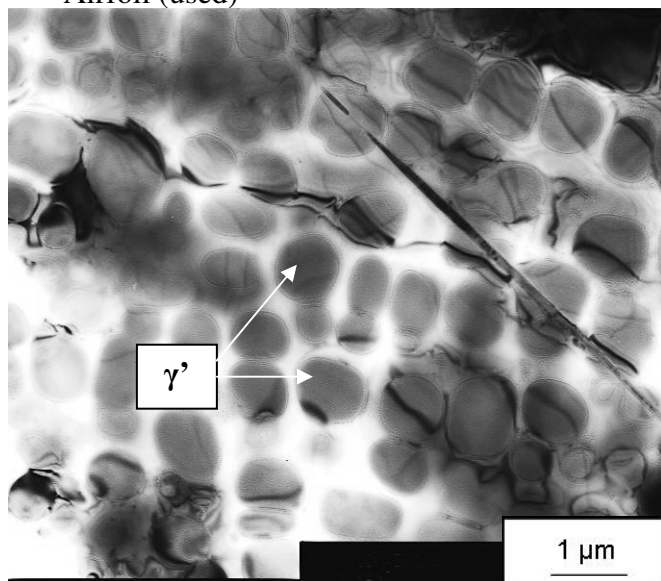


Figure 4.31 - TEM micrograph of airfoil sample. Notice spherical γ' in γ matrix. Electron diffraction pattern for γ' (FCC). $B = [111]$

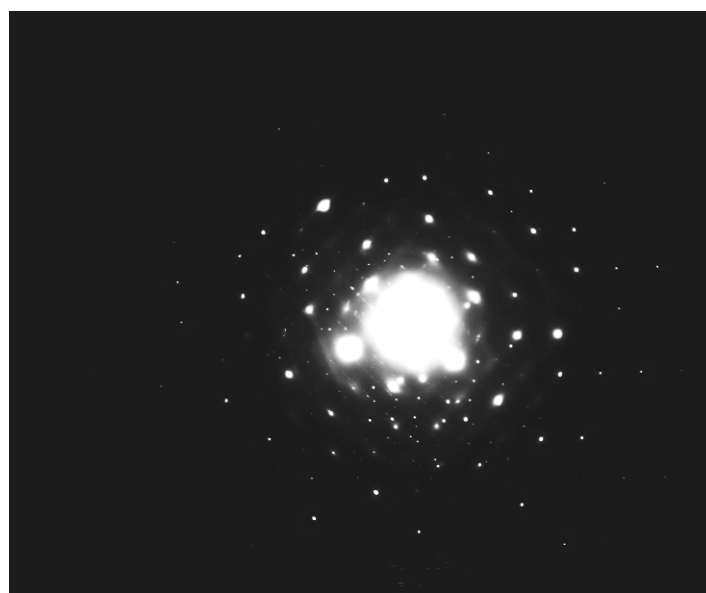
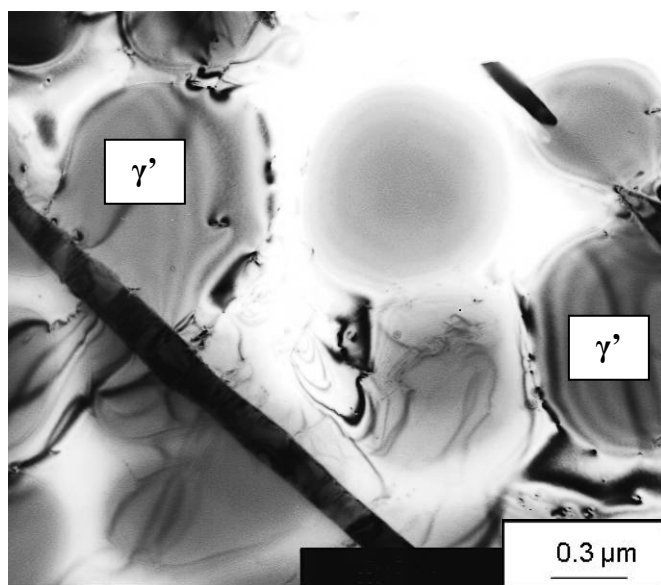


Figure 4.32 - TEM micrograph of airfoil sample. Notice spherical γ' and $M_{23}C_6$ in γ matrix. Electron diffraction pattern for γ' (FCC). $B = [100]$ outer portion of pattern.

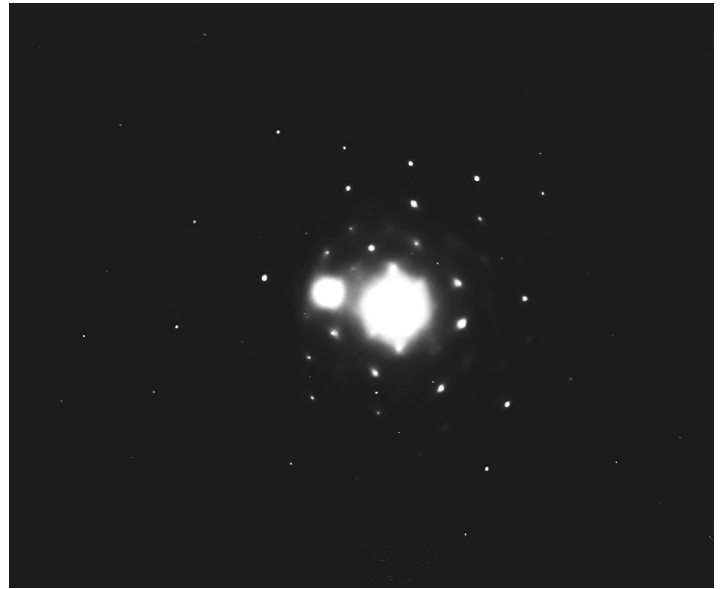
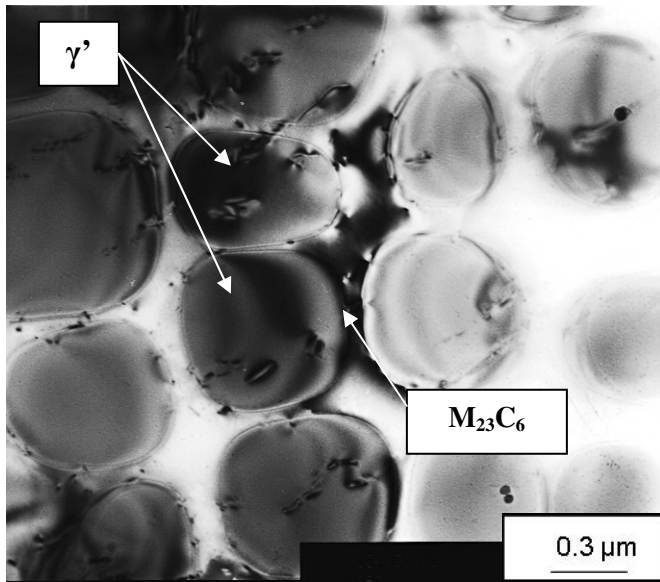


Figure 4.33 - TEM micrograph of airfoil sample. Notice spherical γ' and $M_{23}C_6$ in γ matrix. Electron diffraction pattern for γ' (FCC). B = [013] outer portion of pattern.

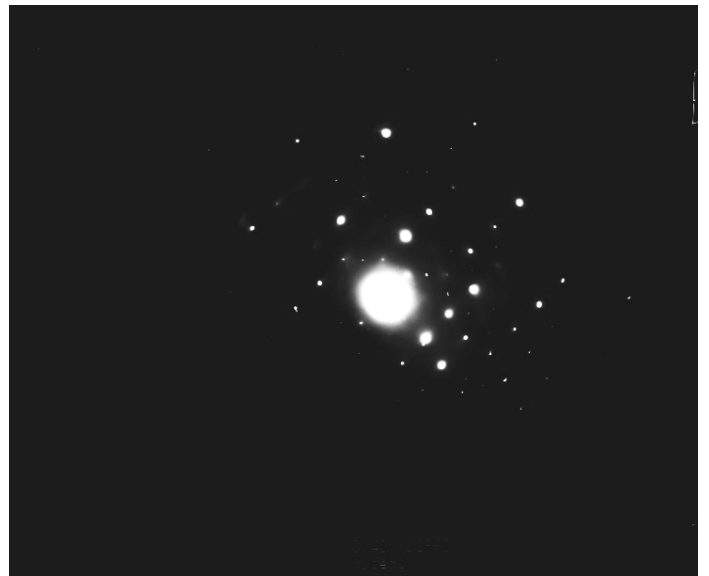
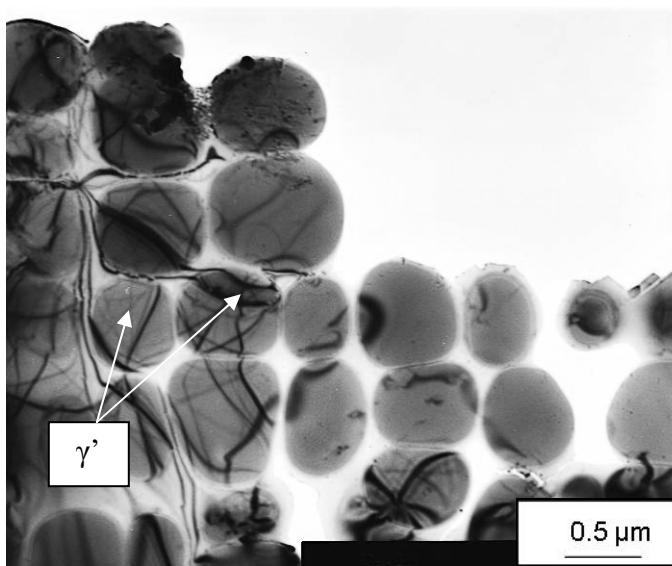


Figure 4.34 - TEM micrograph of airfoil sample. Notice spherical γ' in γ matrix. Electron diffraction pattern for γ' (FCC). B=[001].

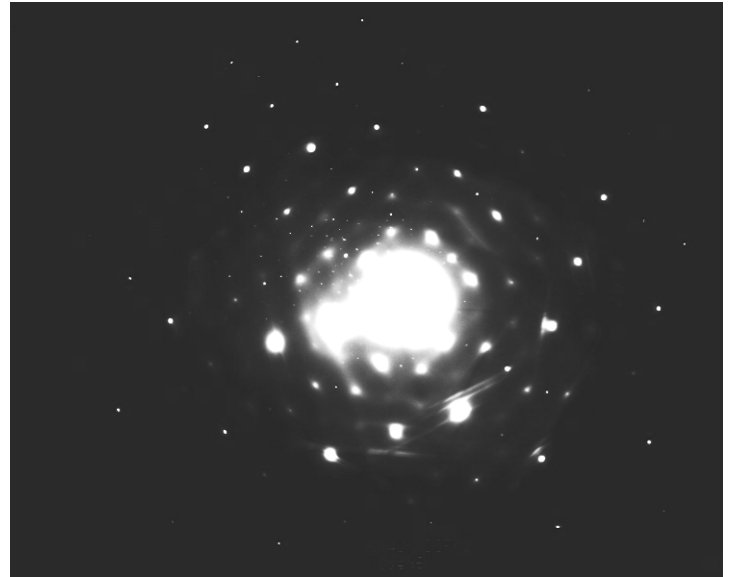
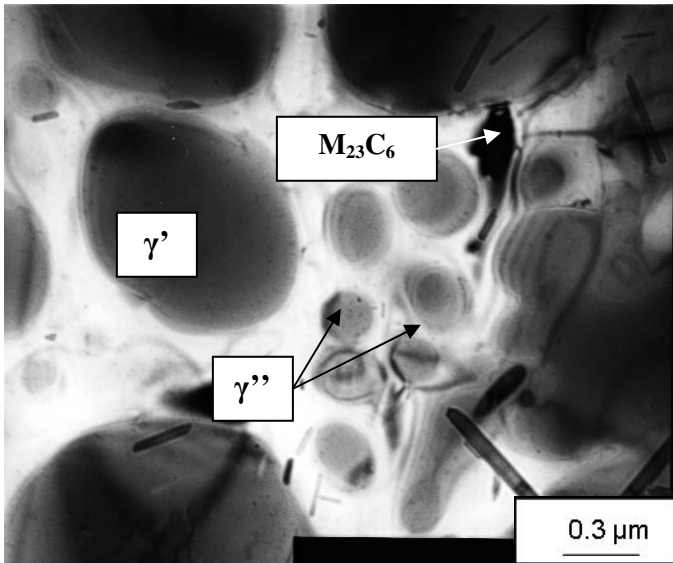


Figure 4.35 - TEM micrograph of airfoil sample. Notice spherical γ' , γ'' , and $M_{23}C_6$ in γ matrix. [27].
Electron diffraction pattern for γ'' (bct).

Chapter 5: Discussion

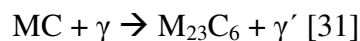
5.1 Microstructural Analysis

The microstructures and phase compositions of the shank sample did not change significantly during service. Its primary microstructure is mainly formed by the γ matrix with a strengthening phase of γ' (cuboidal shape) and few MC carbide islands and eutectic phases throughout the sample. The microstructure of the airfoil sample changed significantly once exposed to the aforementioned service conditions. The γ' coarsened and its shape changed from cuboidal to almost spherical morphology. In some areas, the γ' particles coalesced forming a network, which is detrimental to the alloy's properties. MC carbide islands mostly decomposed into $M_{23}C_6$ carbides that settled throughout the grain boundaries. The γ' growth and morphological alteration depends on diffusion under severe temperatures that it results in the agglomeration of γ' particles while the mismatch ratio γ'/γ increases, which results in an increase of the strain energy from the interface and the γ' becomes unstable [28].

Such $M_{23}C_6$ precipitation on the grain boundaries caused by high temperature exposure can have negative effects depending on their morphology. If they precipitate as a continuous grain boundary film, properties will be degraded. They can reduce carbon content to low levels thus reducing creep life and ductility [29]. M_6C carbides are formed when molybdenum or tungsten replace chromium. Since they are more stable than the $M_{23}C_6$ carbides, they are more beneficial as a grain boundary precipitate to control grain size. MC carbides decompose into $M_{23}C_6$ and M_6C once exposed to high temperatures (760°C - 980°C), but long time exposure can make M_6C decompose back to $M_{23}C_6$ [30], which if precipitated as continuous grain boundary film, can be detrimental to the material's properties as previously discussed.

5.2 Elemental Composition (EDS)

The decomposition of the MC carbides is described as:



In the service exposed airfoil sample, the MC decomposition slowly yields carbon into the γ matrix forming chromium-rich $M_{23}C_6$ carbides (Figure 4.14). The carbon concentration increased in the γ matrix and surrounding areas while the nickel and chromium concentration increased in the MC – γ

reaction zone of the airfoil sample. Diffusion is presumed to have taken place since above $0.6T_m$, the γ matrix strengthening is diffusion dependent. Since the operating temperatures for this set of buckets was 1700 – 1800°F (926 – 982°C) and the melting temperature of GTD-111 is approximately 2642° F (1450°C) [32], the γ matrix could have gained strength by diffusion since $0.6T_m = 1585^\circ\text{F}$ (862°C). EDS results are not as fully representative of what actually takes place due to factors such as homogeneity in the chemical composition of the bucket prior to service is not known and the absence of EDS standards. The chemical presence of chromium, aluminum, tungsten and titanium in the γ matrix of the airfoil sample increased after being exposed to high temperature service conditions (1700 – 1800°F; 926 – 982° C) (Figure 4.12). The increase of such chemical concentrations suggests that chromium and titanium diffused from the γ matrix into the MC carbide (i.e. $M_{23}C_6$) [33]. It also involves the exchange of solute atoms between the precipitates and surrounding γ matrix. Aluminum is a good solid solution strengthener, but also molybdenum, chromium, and tungsten can also contribute to the strengthening of the alloy via solid solution (cobalt, chromium, molybdenum, tungsten, titanium, and aluminum being the solute elements) [34]. More slowly diffusing elements to include molybdenum and tungsten would be the strongest hardeners [35]. Chromium, molybdenum, tungsten, aluminum, and cobalt are present in solid solution in the γ matrix, which has a FCC crystal structure. The γ' phase has an ordered FCC structure of $Ni_3(Al, Ti)$ but chromium can substitute for some of the nickel. Vacancy diffusion can take place between the γ and γ' once the $0.6T_m$ threshold is reached. Strengtheners such as aluminum, titanium, tungsten, and chromium could have diffused into the γ matrix and/or γ' and strengthened the alloy as indicated in the hardness results (Figures 4.18, 4.20, 4.21, 4.22, and 5.36). The chemical presence of the solutes increased in the γ matrix, γ' phase, and MC carbides as seen in the EDS results thus causing the aforementioned hardness increase. It is important to mention that these EDS results are purely qualitative and do not consider chemical composition variations such as homogenization effects or other variables in the chemical composition.

By means of optical microscopy, eutectic phase regrowth appeared to be larger in the shank sample than in the airfoil sample possibly due to the casting process (geometry variations, cooling rates). There is also a possible vacancy diffusion within the γ/γ' eutectic phase interface. It is important to mention that the original size and shape of the eutectic phases in the shank could not be determined due

to the shank's "used condition", so no reference point can be established. The possible diffusion could have also contributed to a decrease in size of the eutectic phases mainly due to the vacancy diffusion occurring between the eutectic phases and γ matrix of the airfoil due to the high temperature exposure (i.e. the γ matrix strengthening being diffusion dependant above $0.6T_m$, = 1585°F. Operating service temperature was between 1700 - 1800°F). When superalloys are heat treated, the composition of the γ' phase must be changed, so that in the precipitate free zone at the periphery of coarse γ' , diffusion in the surrounding matrix can occur [36]. Elements (aluminum and titanium) in the eutectic phase in the airfoil sample have a lower elemental presence than the shank sample, which can be attributed to its natural composition (excess γ' , carbides, borides, and low melting phases) [37] (Figures 4.15, 4.16). It is important to mention that even though these components are premium castings, it is possible, that even with homogenization, that the chemical composition was not uniform. Also, while energy dispersive x-ray spectroscopy (EDS) is precise, the results are purely qualitative since standards were unavailable for this research.

5.3 Hardness Results

Hardness for the shank sample ranged between 392 HV and 447 HV. Microhardness from the airfoil sample (exposed to heat) saw a range of 447 HV – 485 HV in the airfoil (tip area) and a 392 HV – 447 HV range in the area towards the leading edge. It can be seen that the area exposed to heat (airfoil – area 1) the microhardness increased approximately 6%, due to the increase in size of the γ' particles during service of the bucket. The γ' diameter in the airfoil sample increased compared to the shank sample. The airfoil sample showed a significant increase of the γ' diameter and the γ' coalesced thus decreasing its original properties (i.e. creep resistance). As seen in Figure 5.36, the hardness can be related to the ultimate tensile strength (UTS) which shows a difference between the shank and the Area 1 (A1) of the airfoil, while the shank and Area 2 (A2) and Area 3 (A3) remain in the same range. UTS values for GTD-111 at room temperature (21°C) range between 953 – 1011 MPa [38], while the rest of the areas (A2, A3, and shank) fall in that range, suggesting that those areas have a lower thermal exposure.

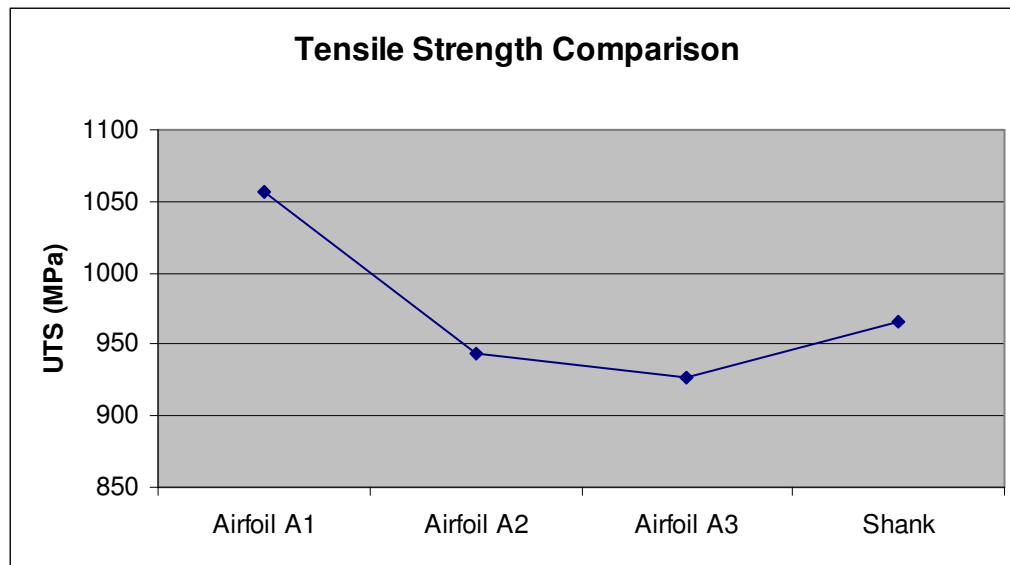


Figure 5.36 Tensile strength comparison between areas of airfoil and shank sections.

An increase in the diameter of the γ' particles was observed by Scanning Electron Microscopy (SEM) in the airfoil area. The γ' precipitates coalesced and coarsened considerably as seen in the size increase of the γ' precipitates (Figure 4.25). The diameter was measured radially using scanning electron microscopy. Also, when a stress (in this case, a centrifugal stress is being applied due to the rotating nature of the bucket's operation) is applied during high temperature exposure (1700 – 1800°F; 926 – 982° C), rafting occurs and depends on the direction of the applied stress and on the lattice misfit between both matrix and precipitate phase (γ and γ'). The rafts are parallel or perpendicular to the principal stress and its direction depends on whether the stress is tensile or compressive. Rafting leads to the shrinking of the γ' particles along the tensile axis as their transverse dimensions increase (Figure 4.24) [39]. This causes the γ' to have different morphologies and agglomeration variations. Also, the size, shape, and volume fraction of the γ' will be influenced by the cooling rate following service [40].

5.4 Gamma Prime (γ') and Transmission Electron Microscopy

Figures 4.30 through 4.35 show TEM micrographs of the shank and airfoil sections. The shank section features cuboidal γ' in a γ matrix. The cuboidal shape is mostly due to the γ/γ' lattice mismatch and high interfacial energy [41]. The γ' starts coalescing and growing in size due to the Ostwald ripening effect (larger particles are more energetically favored than smaller particles), which is controlled by

volume diffusion of the solute atoms [42]. Once the lattice mismatch starts to decrease, the cuboidal shape starts transforming into a sphere at high temperatures [43] and starts losing coherency between them [44]. The minimization of the interfacial energy is the main driving force for the coarsening of the γ' precipitates [45].

On the airfoil section, the γ' coarsened and lost its cuboidal shape transforming into a more spherical shape, which shows that the airfoil sample suffered degradation due to thermal exposure. The growth of the γ' particles can be predicted using the Lifshitz, Sloyozov and Wagner (LSW) theory, which states that the coarsening process is driven by the reduction in total interfacial energy and the growth kinetics would follow a linear equation [46]:

$$D^3 - D_0^3 = Kt \quad (1)$$

where t is the aging time, K is the rate constant, D and D_0 are the average size of the γ' precipitates before aging ($t=0$) and at time t . In this case, the rate constant was calculated using the average γ' diameters and the time in service conditions (~48,000 hrs). The rate constant was calculated to be $2.034 \times 10^{-27} \text{ m}^3/\text{sec}$. Figure 5.37 shows the results of the coarsening of the γ' using the LSW theory with a theoretical 200,000 hrs of service. Figure 5.38 shows a log plot of the graph in Figure 5.37 correlating the γ' size with time simulating actual service conditions of 150,00 hrs. The γ' coarsening would behave exponentially since the coalescence of the particles would make them bigger in size without following a linear behavior.

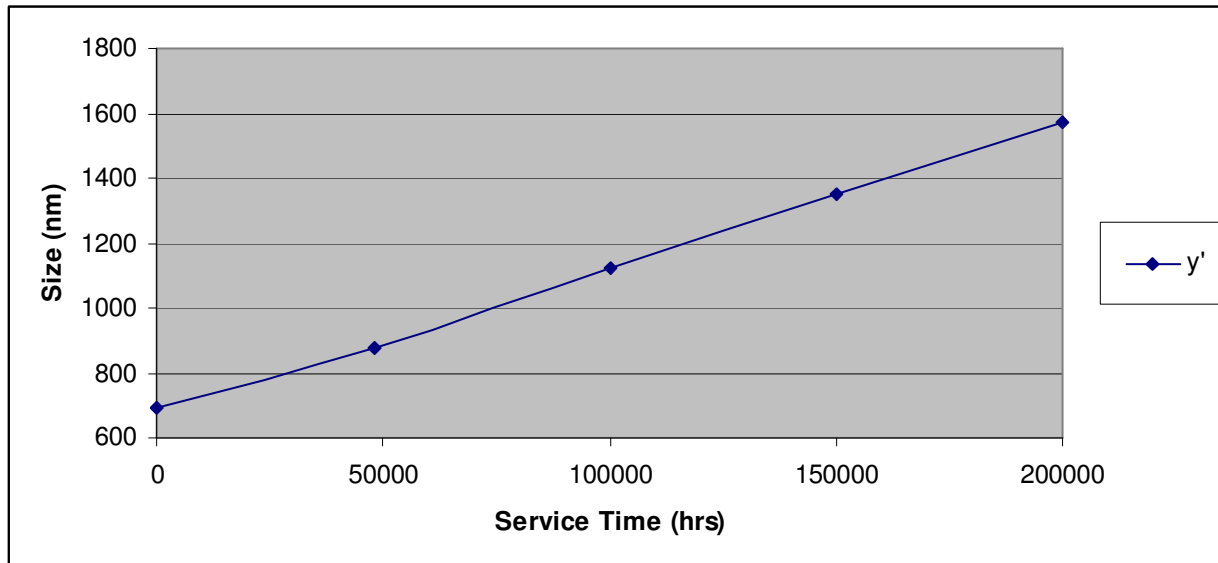


Figure 5.37 Correlation of average size of γ' precipitates with time during service conditions according to LSW theory

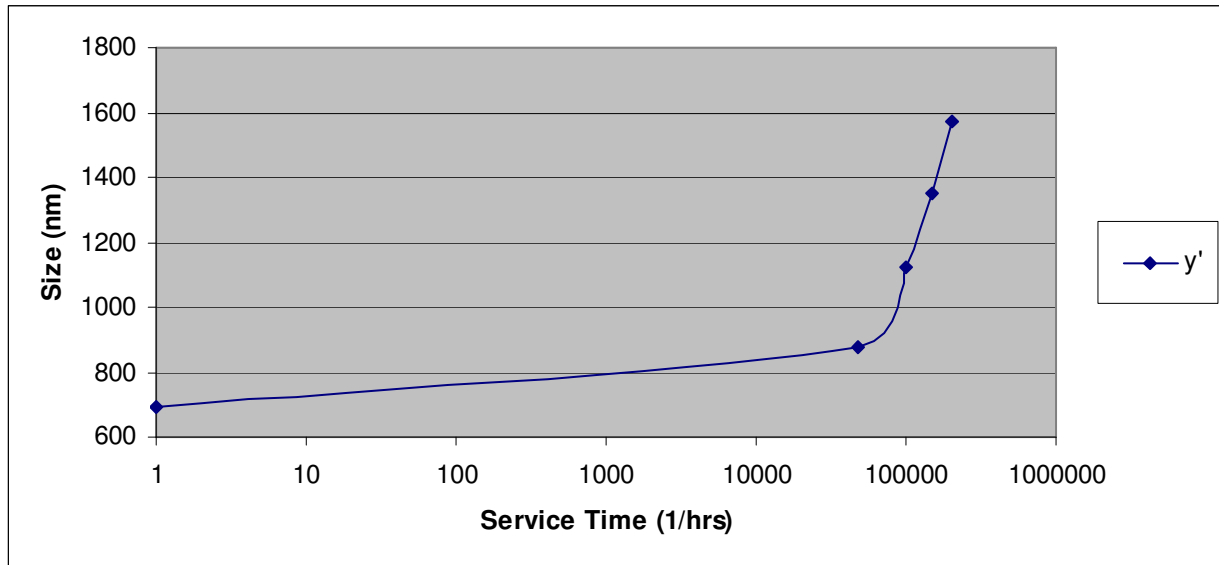


Figure 5.38 Correlation of average size of γ' precipitates with time during service conditions in exponential behavior simulating actual service conditions of 150,000 hrs.

Chapter 6: Conclusions

GTD-111, a Ni-base superalloy, is preferably used for high temperature applications in gas turbine buckets instead of Inconel 738LC since it has better mechanical properties to include creep resistance and higher stress rupture. This study was aimed at the characterization of the microstructural differences that arise between the shank and leading and trailing edges of a GTD-111 gas turbine bucket. A set of 1st stage GTD-111 General Electric Frame 3/2 Model “J” Dry Low NO_x Unit buckets were studied. Two sections of the bucket were studied: airfoil and the shank, which were exposed to service condition temperatures of 1700-1800° F for 48, 064 hours. The shank portion of HP buckets are not exposed to exhaust gases directly and should come close to representing the “original” microstructural state of the entire bucket for reference purposes. In order to examine microstructural and microchemical alteration of the buckets, comparing the airfoil to the platform or shank region, microstructural analysis, microhardness testing, scanning electron microscopy/metallography, elemental composition with energy dispersive x-ray spectroscopy, and transmission electron microscopy analyses were used.

Microstructural changes confirmed by metallography, scanning electron microscopy, transmission electron microscopy, and microhardness testing in the airfoil includes:

- γ' coarsening and particle coalescence,
- the essence of solute re-distribution between the γ and γ' phases, and MC carbide decomposition.
- the apparent thermal modification in γ' eutectic structures.
- and the strengthening of the trailing edge regions of the airfoils.

γ' coarsening and coalescence was confirmed by metallography, SEM, and TEM in the airfoil sample. The overall γ' coarsening occurs mainly by the Ostwald ripening effect and Lifshitz, Sloyozov, and Wagner (LSW) theory, which states that the coarsening is due to the minimization of the interfacial energy and follows a linear behavior (Eq. 1). Also, once the lattice mismatch between the γ and the γ' phases starts decreasing, coherency is lost and the cuboidal shape of the γ' starts transforming into a sphere at high temperatures.

Chemical variations such as a higher presence of elements such as chromium, aluminum, and tungsten were detected by EDS in the γ matrix of the airfoil compared to the γ matrix of the shank. Such variations were also detected in the γ' phase of the airfoil (higher presence in aluminum, tungsten, and titanium) compared to the γ' phase of the shank). MC carbides also showed variations in the airfoil sample compared to the shank region (higher chromium presence). The eutectic phase of the airfoil showed a lower presence of titanium, aluminum, and tungsten compared to the shank. Even though the chemical variations shown in the EDS results are not quantitative, it is important to mention that diffusion would have taken place (i.e. the γ matrix strengthening being diffusion dependent above $0.6T_m$, = 1585°F and with an operating service temperature between 1700 - 1800°F). It is also important to mention that even though these components are premium castings, it is possible, that even with homogenization, that the chemical composition was not uniform prior to service exposure. Also, while energy dispersive x-ray spectroscopy (EDS) is precise, the results are purely qualitative since standards were not used in this study. These elemental variations were not considered in this research and need to be considered in future work.

All of these elemental changes in the microstructure suggest that vacancy diffusion took place and could have contributed to the strengthening (higher hardness and tensile strength) of the trailing edge of the airfoil. It is important to mention that the enhancement of such properties does not mean that the alloy's performance is going to improve. The material's performance mainly depends on the ability of the alloy to retain its original microstructural features during service, since preserving this microstructural state represents an optimum design condition.

Metallographic inspection by replication in the trailing edge of the blade can be used to analyze the microstructural changes the buckets have undergone (γ' coarsening and coalescence). This technique is non-destructive and can be used in preventive maintenance routines to assess the microstructural degradation that the component has suffered and determine if the component can continue in service.

In terms of future work, a more in depth microstructural investigation could be performed for different service condition exposures since finding a more approximate rate of degradation of the γ' phase can help determine the alloy's remaining service life more precisely. Additional research could also be performed to explore the severity of the microstructural alteration demonstrated by service exposure.

Conceivably solutionizing and aging could restore the components back to their original form providing creep cavity formation was remedied by hot isostatic pressing (HIPing) [47]. Any future work would have to entail creep rupture testing to confirm residual elevated temperature properties.

References

- [1] Bhadeshia, H.K.D.H.. The Superalloys. University of Cambridge; <http://www.msm.cam.ac.uk/phase-trans/2003/nickel.html>; 2003
- [2] Sims, Chester T.; Stoloff, Norman S.; Hagel, William C. Superalloys II. Pg. 97. John Wiley & Sons. 1987.
- [3] Sims, Chester T.; Hagel, William C. The Superalloys. Pg. 17. John Wiley & Sons. 1972
- [4] Sajjadi, S.A; Zebarjad, S.M.; Guthrie, R.I.L.; Isac, Microstructure evolution of high temperature Ni-base superalloy GTD-111 with different heat treatment parameters; Journal of Materials Processing Technology; 2005
- [5] Schilke, P.W. 2004. Advanced Gas Turbine Materials and Coatings. GE Energy. General Electric Company
- [6] Sidhu, R.K.; Ojo, O.A.; Chaturvedi, M.C.; Sub-solidus melting of directionally solidified René 80 superalloy during solution heat treatment; Journal of Materials Science; 2008
- [7] Sajjadi, S.A.; Nategh, S.; A high temperature deformation mechanism map for the high performance Ni-base superalloy GTD-111; Materials Science and Engineering A307 158-164; 2001.
- [8] Schilke, P.W. 2004. Advanced Gas Turbine Materials and Coatings. GE Energy. General Electric Company
- [9] Abdolkarim Sajjadi, Seyed; Nategh, Said; Guthrie, Roderick I.L.; Study of Microstructure and Mechanical Properties of High Performance Ni-base Superalloy GTD-111; Materials Science and Engineering A325 484 – 489; 2002
- [10] Callister, William D. Fundamentals of Materials Science and Engineering, 5th Edition. Pg 347. John Wiley and Sons. 2000
- [11] Sims, Chester T.; Stoloff, Norman S.; Hagel, William C. Superalloys II. Pg. 66. John Wiley & Sons. 1987.
- [12] Kang, S.K; Benn, R.C; Microstructural Development in High Volume Fraction Gamma Prime Ni-Base Oxide-Dispersion-Strengthened Superalloy; Metallurgical Transactions A; July 1995

- [13] B.G Choi; I.S. Kim; D.H. Kim; C.Y. Jo; Temperature dependence of MC decomposition behavior in Ni-base superalloy GTD 111; Materials Science and Engineering, June 2007.
- [14] Sims, Chester T.; Stoloff, Norman S.; Hagel, William C. Superalloys II. Pg. 102. John Wiley & Sons. 1987.
- [15] Vander Voort, George F.; James, Hughston, M. Wrought Heat-Resistant Alloys. Pg. 305. ASM Handbook Volume 9 “Metallography and Microstructures”. ASM International. 1998.
- [16] Durand-Charre, Madeleine. The Microstructure of Superalloys. Pg 42. CRC Publishing. 1998.
- [17] Vander Voort, George F.; James, Hughston, M. Wrought Heat-Resistant Alloys. Pg. 311. ASM Handbook Volume 9 “Metallography and Microstructures”. ASM International. 1998
- [18] Kountras, Apostolos. Metallographic Study of Gamma – Gamma Prime Structure in the Ni-based Superalloy GTD 111. Massachusetts Institute of Technology. 2004.
- [19] Vander Voort, George F.; James, Hughston, M. Wrought Heat-Resistant Alloys. Pg. 311. ASM Handbook Volume 9 “Metallography and Microstructures”. ASM International. 1998
- [20] Sims, Chester T.; Hagel, William C. The Superalloys. Pg. 54. John Wiley & Sons. 1972
- [21] Vander Voort, George F.; James, Hughston, M. Wrought Heat-Resistant Alloys. Pg. 310. ASM Handbook Volume 9 “Metallography and Microstructures”. ASM International. 1998
- [22] Sims, Chester T.; Hagel, William C. The Superalloys. Pg. 55. John Wiley & Sons. 1972
- [23] Sims, Chester T.; Stoloff, Norman S.; Hagel, William C. Superalloys II. Pg. 115. John Wiley & Sons. 1987.
- [24] Zou, J.; Wang, H.P.; Doherty, R.; Perry, E.M.; Solidification Behavior and Microstructure Formation in a Cast Nickel Based Superalloy: Experiment and Modeling; GE Research and Development Center; 1992.
- [25] Bathie, William W., Fundamentals of Gas Turbines. Pg. 259. John Wiley & Sons. 1984.
- [26] Lvov, G.; Levit, V.I; Kaufman, M.J; Mechanism of Primary MC Carbide Decomposition in Ni-Base Superalloys; Metallurgical and Materials Transactions A; June 2004; via e-mail.

- [27] Andrews, K.W.; Dyson, D.J.; Keown, S.R.; Interpretation of Electron Diffraction Patterns; Hilger and Watts Ltd.; 1967
- [28] Vaezi, Mohammed; Soleymani, Masoud. Creep Life Prediction of Inconel 738 Gas Turbine Blade. Pg. 1950-1955. Journal of Applied Sciences Vol. 9, Issue 10, 2009.
- [29] Vander Voort, George F.; James, Hughston, M. Wrought Heat-Resistant Alloys. Pg. 311. ASM Handbook Volume 9 “Metallography and Microstructures”. ASM International. 1998
- [30] Sims, Chester T.; Stoloff, Norman S.; Hagel, William C. Superalloys II. Pg. 116. John Wiley & Sons. 1987.
- [31] Lvov, G.; Levit, V.I; Kaufman, M.J; Mechanism of Primary MC Carbide Decomposition in Ni-Base Superalloys; Metallurgical and Materials Transactions A; June 2004
- [32] Gigliotti, M.F.X.; Huang, S.C.; Klug, F.J.; Ritter, A.M.; GE Casting Project; General Electric Corporate Research and Development
- [33] Lvov, G.; Levit, V.I; Kaufman, M.J; Mechanism of Primary MC Carbide Decomposition in Ni-Base Superalloys; Metallurgical and Materials Transactions A; June 2004
- [34] Kountras, Apostolos. Metallographic Study of Gamma – Gamma Prime Structure in the Ni-based Superalloy GTD 111. Massachusetts Institute of Technology. 2004
- [35] Sims, Chester T.; Stoloff, Norman S.; Hagel, William C. Superalloys II. Pg. 104. John Wiley & Sons. 1987.
- [36] Jianting, Guo; Ranucci, D.; Gherardi, F.; Precipitation of β phase in the γ' particles of nickel base superalloy; Metallurgical Transactions A; Volume 15A; July 1984
- [37] Davis, Joseph R.; Heat Resistant Materials; Pg. 250; ASM International Handbook Committee; 1997
- [38] Daleo, J.A.; Wilson, J.R.; GTD111 Alloy Material Study; Journal of Engineering for Gas Turbines and Power; April 1998.
- [39] Nabarro, Frank R.N.; Rafting in superalloys; Metallurgical and Materials Transactions A; March 1996

- [40] Sajjadi, S.A; Zebarjad, S.M.; Guthrie, R.I.L.; Isac, Microstructure evolution of high temperature Ni-base superalloy GTD-111 with different heat treatment parameters; Journal of Materials Processing Technology; 2005
- [41] Durand-Charre, Madeleine; The Microstructure of Superalloys; Pg. 83. Gordon and Breach Science Publishers. 1997.
- [42] Kim, H.T.; Chun, S.S.; Yao, X.X.; Fang, Y.; Gamma prime precipitating and ageing behaviors in two newly developed nickel-base superalloys; Journal of Materials Science 32; 1997
- [43] Loomis, W.T.; Freeman, J.W.; Sponseller, D.L.; The influence of molybdenum on the γ' phase in experimental nickel base superalloys; Metallurgical Transactions; 1972
- [44] Zhao, Shuangqun; Xie, Xishan; Smith, Gaylord D.; Patel, Shailesh J.; Gamma prime coarsening and age-hardening behaviors in a new nickel base superalloy; Materials Letters 58; Pg. 1784-1787; 2004.
- [45] Durand-Charre, Madeleine; The Microstructure of Superalloys; Pg. 83. Gordon and Breach Science Publishers. 1997
- [46] Moshtaghin, R.S.; Asgari, S.; Growth kinetics of γ' precipitates in superalloy IN-738LC during long term aging; Materials and Design 24; Pg. 325-330; 2003
- [47] Baldan, A.; Rejuvenation procedures to recover creep properties of nickel-base superalloys by heat treatment and hot isostatic pressing techniques; Journal of Materials Science 26; 1991

Curriculum Vita

Oscar Quintero was born on March 28th, 1982, in Ciudad Juárez, Chihuahua, Mexico. The oldest son of Oscar Quintero Milán and Teresa de Jesús Soltero Aguirre. Oscar attended elementary, middle school, and high school in Ciudad Juárez. He graduated from the University of Texas at El Paso (UTEP) as an electrical engineer with the option in semiconductors. While attending college, he worked at UTEP as a system administrator, computer technician, and as an undergraduate research assistant. He also worked at Delphi Automotive Systems as a Materials Engineer / Failure Analyst in the Materials Engineering Laboratory for almost three years.

People wishing to communicate with Oscar can write to his permanent home address:

Quinta Alegre #8628, Fracc. Las Quintas, Ciudad Juárez, Chihuahua, México. C.P. 32400.

Permanent address: Quinta Alegre #8628
Fraccionamiento Las Quintas
Cd. Juárez, Chih., México, C.P. 32400

This thesis was typed by Oscar Quintero Soltero